Dalton Transactions

ROYAL SOCIETY OF CHEMISTRY

PAPER

View Article Online
View Journal | View Issue

Check for updates

Cite this: *Dalton Trans.*, 2022, **51**, 9748

Biomimics of [FeFe]-hydrogenases incorporating redox-active ligands: synthesis, redox properties and spectroelectrochemistry of diiron-dithiolate complexes with ferrocenyl-diphosphines as Fe_4S_4 surrogates†

Georgia R. F. Orton,[a] Shishir Ghosh,[a,b] Lucy Alker,[b] Jagodish C. Sarker,[a] David Pugh,[a] Michael G. Richmond,[c] František Hartl[d] and Graeme Hogarth *[a]

[FeFe]-Ase biomimics containing a redox-active ferrocenyl diphosphine have been prepared and their ability to reduce protons and oxidise H_2 studied, including 1,1′-bis(diphenylphosphino)ferrocene (dppf) complexes $Fe_2(CO)_4(\mu\text{-dppf})(\mu\text{-S(CH}_2)_n\text{S})$ (n = 2, edt; n = 3, pdt) and $Fe_2(CO)_4(\mu\text{-dppf})(\mu\text{-SAr})_2$ (Ar = Ph, p-tolyl, p-$C_6H_4NH_2$), together with the more electron-rich 1,1′-bis(dicyclohexylphosphino)ferrocene (dcpf) complex $Fe_2(CO)_4(\mu\text{-dcpf})(\mu\text{-pdt})$. Crystallographic characterisation of four of these show similar overall structures, the diphosphine spanning an elongated Fe–Fe bond (*ca.* 2.6 Å), lying *trans* to one sulfur and *cis* to the second. In solution the diphosphine is flexible, as shown by VT NMR studies, suggesting that $Fe_2\cdots Fe$ distances of *ca.* 4.5–4.7 Å in the solid state vary in solution. Cyclic voltammetry, IR spectroelectrochemistry and DFT calculations have been used to develop a detailed picture of electronic and structural changes occurring upon oxidation. In MeCN, $Fe_2(CO)_4(\mu\text{-dppf})(\mu\text{-pdt})$ shows two chemically reversible one-electron oxidations occurring sequentially at Fe_2 and Fc sites respectively. For other dppf complexes, reversibility of the first oxidation is poor, consistent with an irreversible structural change upon removal of an electron from the Fe_2 centre. In CH_2Cl_2, $Fe_2(CO)_4(\mu\text{-dcpf})(\mu\text{-pdt})$ shows a quasi-reversible first oxidation together with subsequent oxidations suggesting that the generated cation has some stability but slowly rearranges. Both pdt complexes readily protonate upon addition of $HBF_4{\cdot}Et_2O$ to afford bridging-hydride cations, $[Fe_2(CO)_4(\mu\text{-H})(\mu\text{-dcpf})(\mu\text{-pdt})]^+$, species which catalytically reduce protons to generate H_2. In the presence of pyridine, $[Fe_2(CO)_4(\mu\text{-dppf})(\mu\text{-pdt})]^{2+}$ catalytically oxidises H_2 but none of the other complexes do this, probably resulting from the irreversible nature of their first oxidation. Mechanistic details of both proton reduction and H_2 oxidation have been studied by DFT allowing speculative reaction schemes to be developed.

Received 10th February 2022,
Accepted 5th June 2022

DOI: 10.1039/d2dt00419d

rsc.li/dalton

Introduction

The active site of [FeFe]-H_2ases (a) (Chart 1) consists of diiron $[2Fe]_H$ and tetrairon $[Fe_4S_4]_H$ sub-units linked *via* a cysteine moiety. Strong electronic communication occurs between these subunits *via* redox potential levelling,[1,2] which is essential if both electron transfer events required for the interconversion of protons and hydrogen are to occur with a similar driving force.[3] Over the past 20+ years, significant effort has been made to prepare biomimics of this site,[4] although the majority of these do not include a mimic of the Fe_4S_4 cluster, a number of strategies have also been adopted for the inclusion of a second redox centre.[5–10] In 2005, Pickett and co-workers reported the [FeFe]-H_2ase biomimetic (b) (Chart 1, L = 1,3,5-

[a]*Department of Chemistry, King's College London, 7 Trinity Street, London, SE1 1DB, UK. E-mail: graeme.hogarth@kcl.ac.uk*
[b]*Department of Chemistry, University College London, 20 Gordon Street, London, WC1H 0AJ, UK*
[c]*Department of Chemistry, University of North Texas, 1155 Union Circle, Box 305070, Denton, Texas 76203, USA*
[d]*Department of Chemistry, University of Reading, Whiteknights, Reading RG6 6DX, UK*

†Electronic supplementary information (ESI) available: Text, tables and cif files giving details of the X-ray crystallographic structure determinations; atomic coordinates and energies of all optimised stationary points. Some additional electrochemical information and experiments, crystallographic data and computational details. CCDC 2151071 (**3**), 2151142 (**4a**) and 2151143 (**4c**). For ESI and crystallographic data in CIF or other electronic format see DOI: **https://doi.org/10.1039/d2dt00419d**

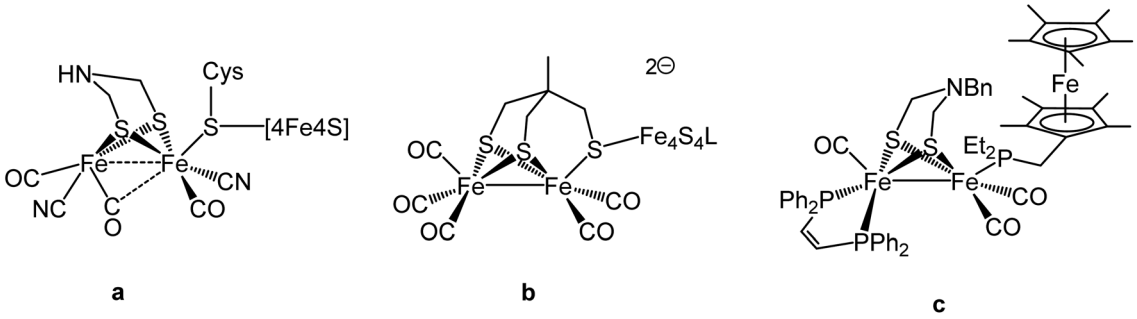

Chart 1

tris((4,6-dimethyl-3-mercaptophenyl)thio)-2,4,6-tris(*p*-tolyl-thio) benzene) containing both Fe_2 and Fe_4 centres, and showed that it functioned as an electrocatalyst for proton-reduction.[6] Later, Camara and Rauchfuss prepared biomimetic (c) (Chart 1, Bn = CH_2Ph) in which the 4Fe–4S cluster is replaced by a permethylated ferrocene linked to the diiron centre through an appended phosphine.[7] The latter was chosen as the redox partner as the electron-releasing methyl groups give rise to a significantly lower oxidation potential. Importantly, (c) is oxidised at mild potentials allowing access to a dication in which both the ferrocene and diiron centres are oxidised, which cleaves dihydrogen.

An attractive Fe_4S_4 surrogate is commercially available, 1,1′-bis(diphenylphosphino)ferrocene (dppf), which shows well-defined Fe(II)/Fe(III) redox chemistry.[11] In 2014 we reported our preliminary findings on the synthesis, electrochemistry and electrocatalysis of $Fe_2(CO)_4(\mu\text{-dppf})(\mu\text{-pdt})$ (**1**).[8] Herein we develop this chemistry. Our initial goal was to coordinate dppf in a chelating fashion to a single iron atom, *viz.* to prepare $Fe_2(CO)_4(\kappa^2\text{-dppf})(\mu\text{-dithiolate})$, since unsymmetrically substituted chelate complexes have been predicted to be the best electrocatalysts.[12] Indeed, in related studies with $Ph_2PN(R)PPh_2$-functionalised biomimics, we have shown experimentally that chelate isomers are more efficient electrocatalysts than bridged analogues.[13] Unfortunately, we have not been able to realise this, but have successfully prepared a small number of other dppf-bridged diiron complexes with both dithiolate and bis(dithiolate) bridges and these together with detailed electrochemical and spectroelectrochemical (SEC) studies on their oxidation chemistry are described herein.

Results and discussion

Reactions of $Fe_2(CO)_6(\mu$-dithiolate) with 1,1′-bis(diphenylphosphino)ferrocene (dppf) and 1,1′-bis(dicyclohexylphosphino) ferrocene (dcpf)

Our initial aim was to prepare chelate complexes $Fe_2(CO)_4(\kappa^2\text{-dppf})(\mu\text{-pdt})$ and $Fe_2(CO)_4(\kappa^2\text{-dcpf})(\mu\text{-pdt})$ as this framework closely mimics the active site of [FeFe]-H_2ase.[12] To achieve this, we first explored reaction of *ca.* equimolar amounts of dppf and $Fe_2(CO)_6(\mu\text{-pdt})$ under a variety of experimental conditions. In MeCN with added $Me_3NO{\cdot}2H_2O$, pentanuclear $\{Fe_2(CO)_5(\mu\text{-pdt})\}_2(\mu\text{-}\kappa^1,\kappa^1\text{-dppf})$[14] rapidly formed in high yields but heating at 70 °C for 6 h resulted in no significant change. In refluxing toluene, the reaction was slow, and after 24 h a $^{31}P\{^1H\}$ NMR spectrum showed a series of signals attributed to the presence of $\{Fe_2(CO)_5(\mu\text{-pdt})\}_2(\mu\text{-}\kappa^1,\kappa^1\text{-dppf})$ (55.4 ppm),[14] dppf (−16.9 ppm), a signal at −17.4 ppm tentatively assigned to $Fe_2(CO)_5(\kappa^1\text{-dppf})(\mu\text{-pdt})$ and $Fe_2(CO)_4(\mu\text{-dppf})(\mu\text{-pdt})$ (**1**) (51.3 ppm). Refluxing the mixture for a further 4 d resulted in the disappearance of all signals apart from that associated with **1** and removal of volatiles followed by washing with hexanes gave **1** as a dark red solid in 52% yield (Scheme 1). In a separate experiment, we found that heating $\{Fe_2(CO)_5(\mu\text{-pdt})\}_2(\mu\text{-}\kappa^1,\kappa^1\text{-dppf})$ (**X**)[14] with dppf in refluxing toluene also gave **1**. The most expedient preparation of **1** was found to be from heating $Fe_2(CO)_6(\mu\text{-pdt})$ and dppf in xylene over 1 d, although yields (48%) are slightly lower than from toluene. While this work was in progress, Li and co-workers independently reported the synthesis of $Fe_2(CO)_4(\mu\text{-dppf})(\mu\text{-}SCH_2CHPhCH_2S)$,[15] from reaction of $Fe_2(CO)_6(\mu\text{-}SCH_2CHPhCH_2S)$ with dppf, its formation also proceeding *via* an initially formed pentanuclear intermediate.

Heating $Fe_2(CO)_6(\mu\text{-pdt})$ and dcpf in refluxing toluene, even over prolonged periods, gave no evidence of $Fe_2(CO)_4(\mu\text{-pdt})(\mu\text{-dcpf})$ (**2**) formation, but **2** could be isolated (55% yield) upon refluxing $Fe_2(CO)_6(\mu\text{-pdt})$ and dcpf in xylene for 16 h. No intermediate(s) were observed, and the reaction was not affected by addition of Me_3NO. It is not clear why this is the outome, especially given the facile formation of **X**, but it may be that the bulky dcpf ligand binds to $Fe_2(CO)_6(\mu\text{-pdt})$ in a basal site which is pre-organised for bridge formation. In contrast, substitution of $Fe_2(CO)_6(\mu\text{-pdt})$ and related diiron-dithiolate complexes by dppf occurs at an apical position and for bridge formation an apical-basal isomerisation must occur, which likely has a high activation energy. We also attempted analogous reactions of $Fe_2(CO)_6(\mu\text{-pdt})$ with dipf (R = ^{i}Pr) and dtbpf (R = ^{t}Bu) but in both cases were unable to isolate a stable product (see Experimental section for details).

The synthesis of $Fe_2(CO)_4(\mu\text{-dppf})(\mu\text{-edt})$ (**3**) has been claimed by Li and co-workers,[16] but inspection of their spectroscopic data shows they prepared pentanuclear $\{Fe_2(CO)_5(\mu\text{-edt})\}_2(\mu\text{-}\kappa^1,\kappa^1\text{-dppf})$.[17] We independently prepared this

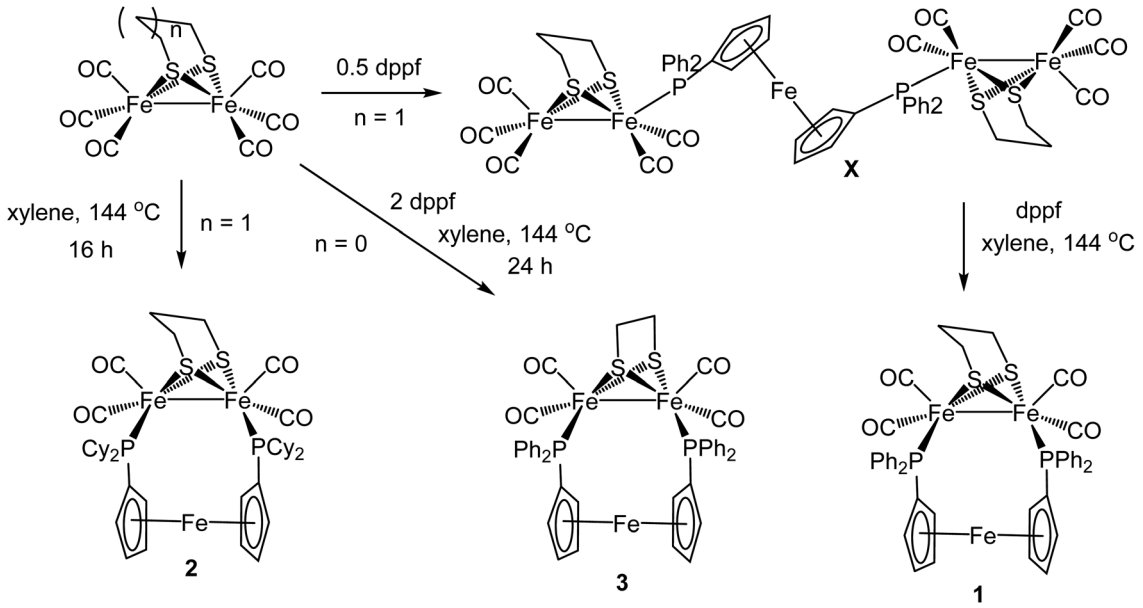

Scheme 1 Synthesis of diphosphine-bridged complexes **1–3**.

complex and heated it in the presence of added dppf but were unable to isolate the μ-dppf product. Similarly, heating $Fe_2(CO)_5(\kappa^1$-dppf)(μ-edt), formed from $Fe_2(CO)_6$(μ-edt) and dppf in MeCN in the presence of the decarbonylation agent Me_3NO,[19] also resulted only in decomposition. We were able to isolate relatively small amounts of **3** (*ca.* 20% yield) upon heating $Fe_2(CO)_6$(μ-edt) and 2 equivalents of dppf in xylene for 24 h. Separation from excess unreacted dppf and other minor products was by thin layer chromatography (TLC), the second band being confirmed as **3**.

IR spectra of **1–3** are characteristic of an $Fe_2(CO)_4$(μ-diphosphine)(μ-dithiolate) motif,[18] the ν(CO) region consisting of four absorptions at 1986s, 1949vs, 1918s 1896w cm^{-1} for **1** and 1974s, 1934vs, 1903s, 1879w cm^{-1} for **2**, the shift to lower wavenumbers of *ca.* 15 cm^{-1} being expected for the more electron-donating dcpf *vs.* dppf ligand. In the ^{1}H NMR spectrum of **1**, four broad singlet resonances of equal intensity between δ 4.93–4.01 are seen for the cyclopentadienyl protons and three broad multiplets between δ 2.60–2.13 for the methylene groups of the dithiolate. The $^{31}P\{^1H\}$ NMR spectrum of **1** shows a singlet at 51.3 ppm but for **2**, no phosphorus signals were observed at room temperature and only broad, uninformative, signals were seen in the ^{1}H NMR spectrum, both being dynamically involved with a fluxional process (see later). The edt complex **3** has a characteristic pattern of ν(CO) bands at 1989s, 1952vs, 1921s and 1900w cm^{-1}, and a singlet is seen in the $^{31}P\{^1H\}$ NMR spectrum at 54.9 ppm.

Synthesis of $Fe_2(CO)_4$(μ-dppf)(μ-SC_6H_4-*p*-R)$_2$

To further expand the range of dppf-bridged diiron complexes, we explored reactions of the bis(thiolate) complexes, $Fe_2(CO)_6$(μ-SC_6H_4-*p*-R)$_2$ (R = H, Me, NH_2), with dppf. In xylene at 120–145 °C for *ca.* 30–60 min $Fe_2(CO)_4$(μ-dppf)(μ-SC_6H_4-*p*-R)$_2$ (**4a–c**) were formed in moderate yields after work up (Scheme 2). The ν(CO) pattern is again characteristic, and the ^{1}H NMR spectrum of **4c** shows a broad peak at δ 2.72 attributed to the amine while **4b** shows two sharp methyl singlets assigned to the inequivalent thiolate ligands. The (relatively) rapid formation of **4a–c** is in stark contrast to the slow formation of **1–2** suggesting these reaction reactions proceed *via* a different pathway, and no evidence of a dppf-linked pentanuclear intermediate was observed in the open-bridged complexes.

Solid-state structures

Molecular structures of **1** (Fig. 1a),[8] **3** (Fig. 1b), **4a** (Fig. 1c) and **4c** (Fig. 1d) have been elucidated by X-ray crystallography and selected bond lengths and angles are given in Table 2. Each contains a diiron core spanned by dppf and dithiolate ligands. Iron–iron bond lengths of >2.61 Å are elongated as compared to related $Fe_2(CO)_4$(μ-diphosphine)(μ-dithiolate) complexes, which typically range between 2.46–2.53 Å^3. They are similar to that of 2.6246(3) Å in $Fe_2(CO)_4\{\mu$-$Ph_2P(CH_2)_4PPh_2\}$(μ-pdt)[20] which also contains a highly flexible backbone. This highlights the soft nature of the Fe–Fe contact in these complexes, being easily distorted by the steric requirements of the bridging ligand(s). Diphosphine coordination results in the inequivalence of the two thiolate bridges, the dppf ligand lying *trans* to one and *cis* to the second. In **4c** the aryl substituents adopt a relative *anti*-conformation as noted for other diphosphine complexes of this type such as $Fe_2(CO)_4$(μ-dppm)(μ-$SAr_2)_2$.[21] The iron centre in the ferrocene is quite remote from the diiron centres with $Fe_2\cdots$Fc distances ranging from 4.5–4.7 Å. Molecular structures of **1–2** are similar to those reported for $Fe_2(CO)_4$(μ-dppf)(μ-$SCH_2CHPhCH_2S$)[15] and $Fe_2(CO)_4$(μ-dppf)$\{\mu$-$SCH_2N(R)CH_2S\}$ (R = CH_2CH_2OH, $CH_2CH_2SC(O)Me$).[22]

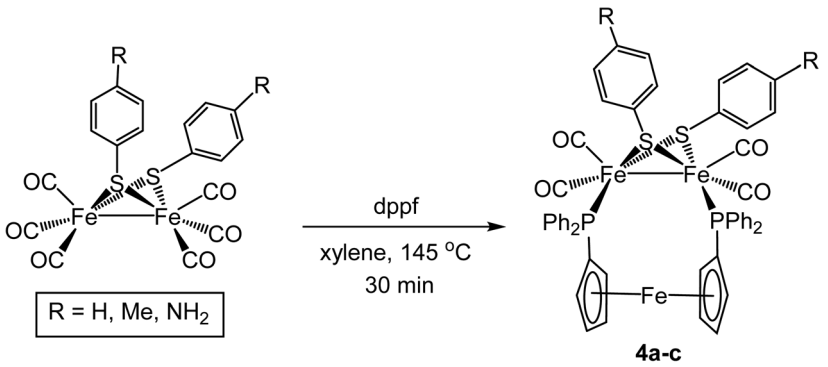

Scheme 2 Synthesis of dppf-bridged complexes **4a–c**.

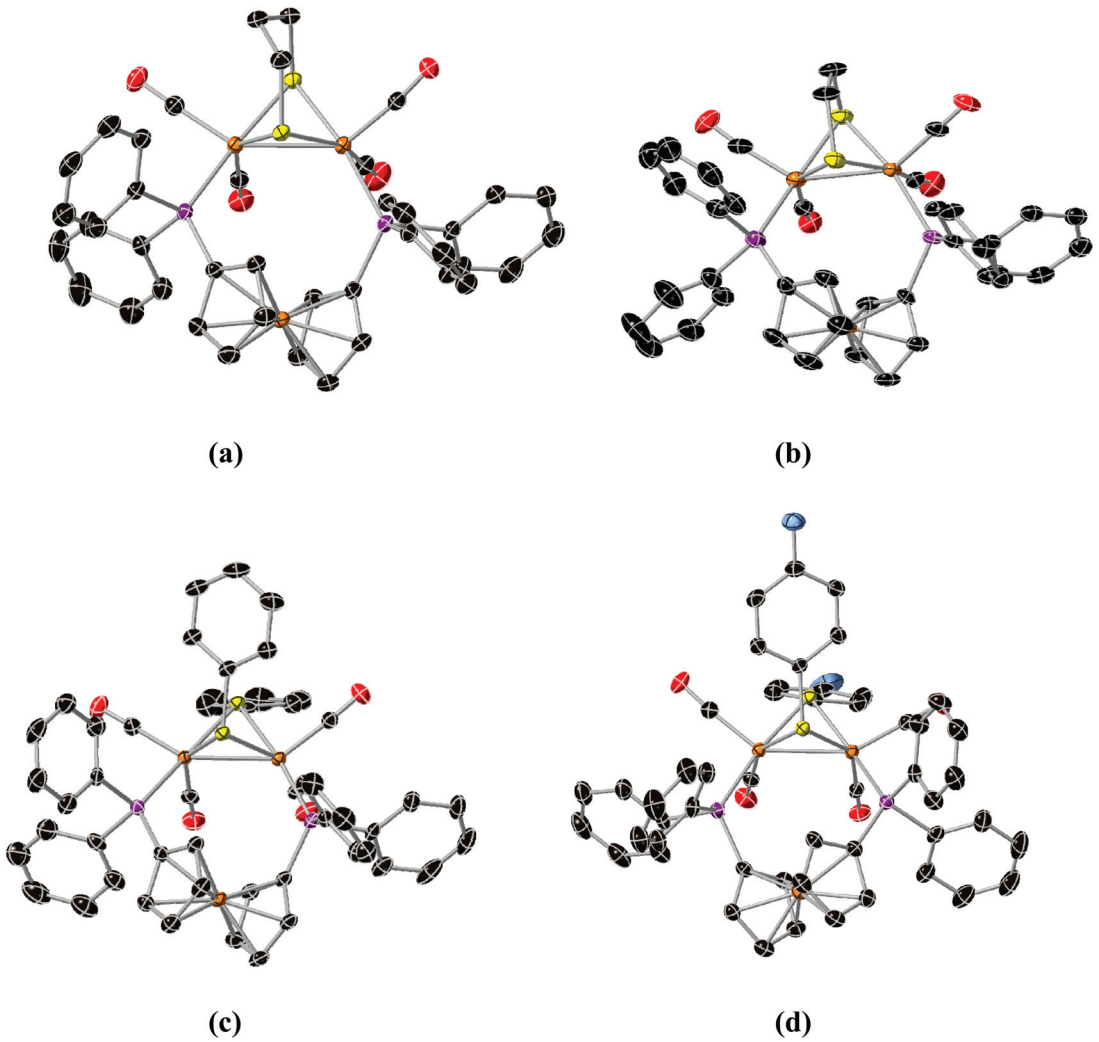

Fig. 1 Molecular structures of (a) **1**, (b) **3**, (c) **4a** and (d) **4c**. Thermal ellipsoids are displayed at 50% probability and hydrogen atoms omitted for clarity.

Solution fluxionality

Dppf has a high degree of conformational flexibility which results from the tilting motion of the two cyclopentadienyl ring planes and a torsional rotation around the Cp–Fe–Cp axis. Consequently, many dppf complexes are fluxional.[23,24] In the solid state, the two ends of the dppf ligand in **1** and **4c** are chemically inequivalent, while in solution at room tempera-

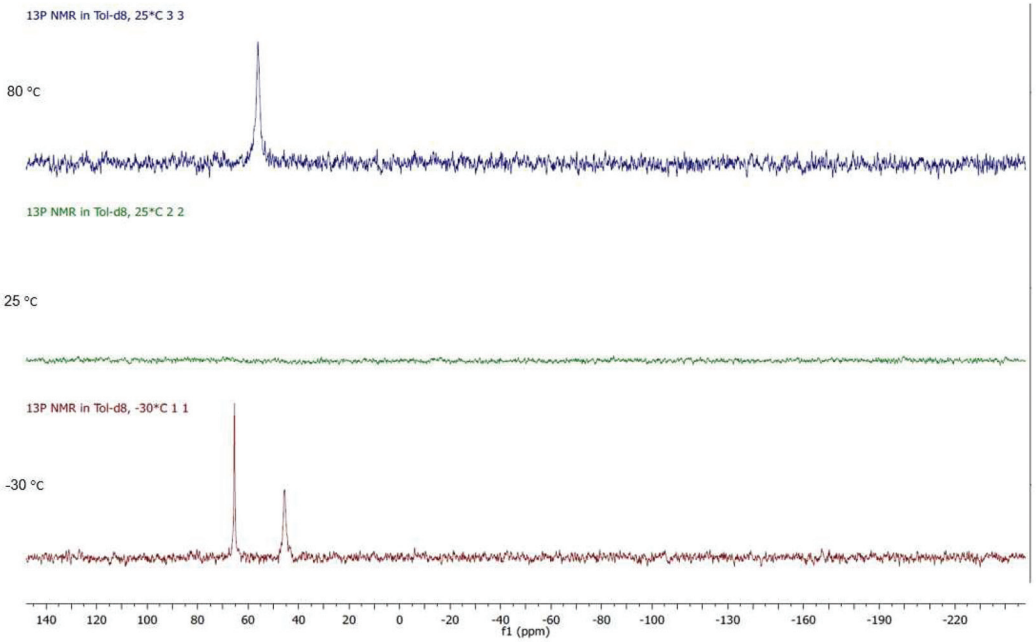

Fig. 2 VT $^{31}P\{^1H\}$ NMR of **2** in toluene-d_8 between −30 and 80 °C.

ture a singlet is observed suggesting they are equivalent, being associated with the flexibility of the dppf ligand. For **2**, in the $^{31}P\{^1H\}$ NMR spectrum at room temperature no signals were seen (Fig. 2), however, upon cooling to −30 °C two phosphorus signals appeared, their difference in linewidth suggesting that an additional fluxional process may still be occurring, being most probably "flipping" of the pdt bridgehead.[25] Warming to 80 °C resulted in coalescence of these signals, as shown by the appearance of a sharp singlet. Non-equivalence of the two phosphorus environments renders the iron centres inequivalent.

Non-equivalence of the two phosphorus atoms and dibasal coordination of the diphosphine should lead to all eight ferrocenyl protons being inequivalent. In the room temperature ^1H NMR spectrum of **2** (Fig. 3) all cyclohexyl and methylene protons appear below 2.8 ppm and the spectrum is difficult to interpret. A broad feature centred at 4.5 ppm is assigned to protons 1/1′ and 4/4′ which interconvert on the NMR timescale. Upon reducing the temperature to −30 °C, separate resonances for protons 1 and 4 are seen at 5.45 and 5.04 ppm respectively, while resonances for 1′ and 4′ overlap at 3.85 ppm. The larger $\Delta\delta$ between 1/1′ as compared to 4/4′ might be explained by the proximity of 1/1′ to the dithiolate bridge. At 80 °C, the other four ferrocenyl protons appear as a single peak, which splits into a 'pseudo doublet' upon cooling at 25 °C due to slowed wagging of the diphosphine (slower 2 → 2′ and 3 → 3′ conversions). The two peak maxima correspond to the overlapping signals of 2 and 3, and 2′ and 3′. Increased broadening of this peak at −30 °C indicates freezing out of these four very similar environments. In is worth noting that the two conformers of the dithiolate bridgehead are not frozen out at temperatures reached in this experiment.

We also carried out VT ^1H NMR studies of **1** and **4b** and see changes in the cyclopentadienyl region of the spectrum consistent with dppf twisting. Importantly, in **4b** the two methyl resonances do not change with temperature, showing that the fluxional process is not associated with the movement of the diphosphine from one side of the molecule to the other, *via* a so-called double trigonal twist process, as has been observed for $Fe_2(CO)_4$(μ-dppm)(μ-dithiolate).[26] Thus, in solution the dppf and dcpf ligands in these complexes are highly flexible.

DFT calculations on bridge and chelate isomers of $Fe_2(CO)_4$(μ-pdt)($Me_2PC_5H_4FeC_5H_4PMe_2$)

In order to better understand why we were unable to isolate (or identify) chelate dppf complexes we have carried out a series of DFT calculations on isomers of $Fe_2(CO)_4$(μ-pdt)($Me_2PC_5H_4FeC_5H_4PMe_2$), replacing phenyl with methyl groups for computational simplicity, while realising that this necessarily underestimates steric considerations. The calculated ground state structure of $Fe_2(CO)_4$(μ-pdt)(μ-$Me_2PC_5H_4FeC_5H_4PMe_2$) (**A**) (Fig. 4a) is in good accord with that found for **1**. The Fe–Fe distance of 2.598 Å is slightly shorter than in **1** (2.6133(6) Å) and the Me_2P groups are staggered somewhat from the normally observed eclipsed geometry in diiron hexacarbonyls, a feature also seen in **2**, and attributed to the low temperature inequivalence of the phosphorus centres.

We also calculated structures for the unobserved dibasal and apical-basal chelate isomers, **A_alt1** and **A_alt2** respectively (Fig. 4b and c). The bridge isomer **A** is thermodynamically favoured, with the dibasal (2.5 kcal mol^{-1}) and apical-basal (5.9 kcal mol^{-1}) ones being higher in energy. Nevertheless, these small energy differences do not eliminate the formation of the chelate isomers solely on thermodynamic grounds.

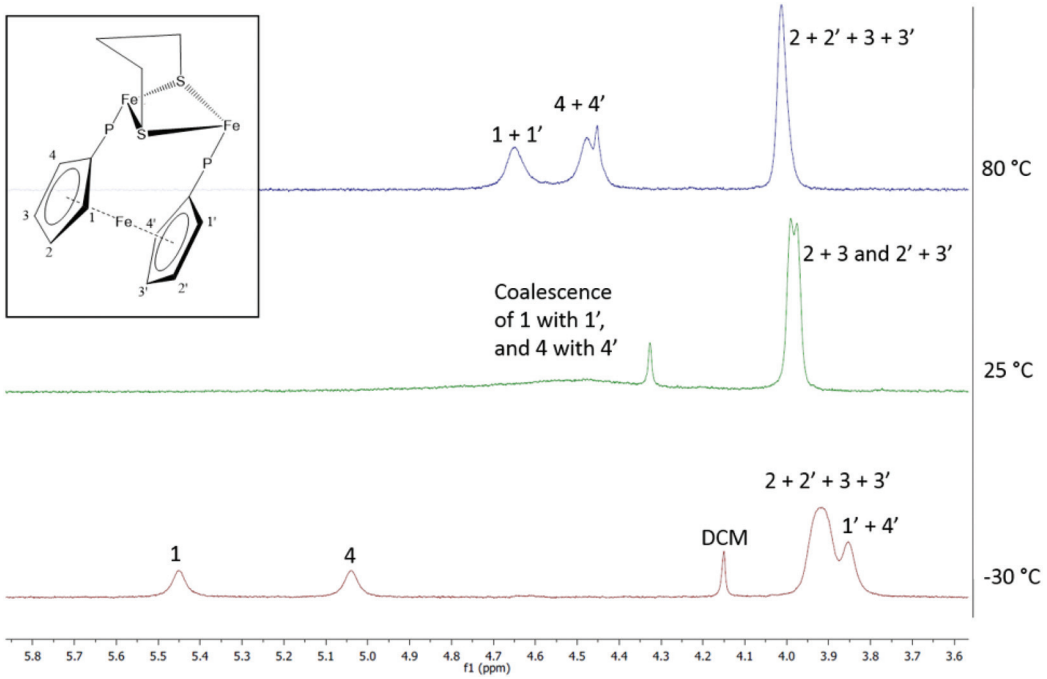

Fig. 3 VT ^{1}H NMR of **2** in toluene-d_8 between −30 and 80 °C.

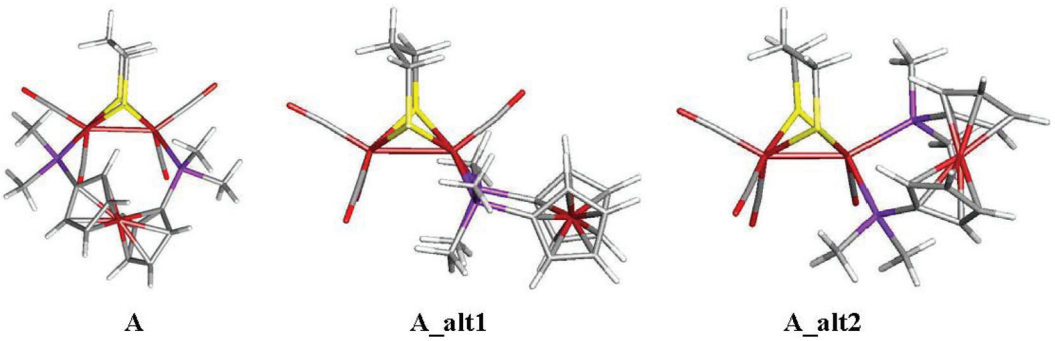

Fig. 4 Ground-state structure of (a) $Fe_2(CO)_4(\mu\text{-pdt})(\mu\text{-}Me_2PC_5H_4FeC_5H_4PMe_2)$ (**A**) and chelate analogues (b) **A_alt1** and (c) **A_alt2**.

For small bite-angle diphosphines such as $Ph_2PC(Me_2)PPh_2$[27] and $Ph_2PN(R)PPh_2$[13] we have shown that chelate isomers are kinetic products of reactions with $Fe_2(CO)_6(\mu\text{-pdt})$ and (slowly) convert to the thermodynamically stable bridge isomers upon heating. A similar chelate-bridge transformation has also been noted for $Os_3(CO)_{10}$(dppf), the chelate complex transforming to the bridge isomer upon heating at 110 °C for 3 h.[23] In the reaction of $Fe_2(CO)_6(\mu\text{-pdt})$ with dppf, initial formation of $Fe_2(CO)_5(\kappa^1\text{-dppf})(\mu\text{-pdt})$ must be quickly followed by addition of a second equivalent of $Fe_2(CO)_6(\mu\text{-pdt})$ to the free phosphorus centre, a low-energy process which is not available to small-angle diphosphine equivalents. Thus, it is this lack of stability of $Fe_2(CO)_5(\kappa^1\text{-dppf})(\mu\text{-pdt})$ under the reaction conditions which precludes formation of chelate complexes.

Cyclic voltammetry (CV) of 1–4

A key feature of [FeFe]-H_2ases is the interaction of Fe_2 and Fe_4S_4 redox centres in the H-cluster. To probe electronic communication between the two redox centres in **1–3** we initially used cyclic voltammetry (CV). Unlike the reversible oxidation–reduction of ferrocene, free dppf undergoes an oxidation at +0.20 V, which is not electrochemically reversible due to the rapid formation of dimeric $[dppf_2]^{2+}$.[11] However, when co-ordinated to a metal centre, oxidation usually becomes chemically reversible and is shifted to more positive potentials.[28]

We first measured CVs of **1** in MeCN at various scan rates (Fig. 5 and Fig. S1†). At 0.1 V s^{-1}, a reversible oxidation at $E_{1/2}$ = +0.05 V (ΔE = 60 mV) and a quasi-reversible oxidation at $E_{1/2}$ = +0.685 V were observed, processes associated with oxi-

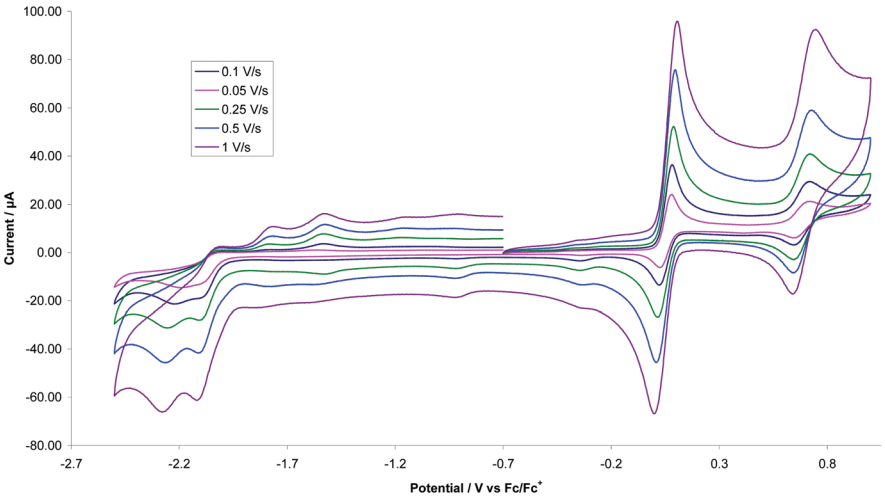

Fig. 5 CVs of **1** at various scan rates in MeCN (1 mM solution, supporting electrolyte $[NBu_4][PF_6]$, glassy carbon electrode, potential *vs.* Fc^+/Fc) scanning positive potential first.

dation of the diiron and ferrocene centres respectively. CVs also show two overlapping irreversible reduction peaks at E_p = −2.10 V and E_p = −2.19 V, which become separated at higher scan rates (≥0.25 V s^{-1}), better separation being observed when the positive potential window was scanned first. Two small oxidation peaks at E_p = −1.80 V and E_p = −1.53 V on the return scan are associated with the product formed in the reductive process, while the small reduction peak at E_p = −0.35 V on the return scan is associated with the first oxidation product. The reversibility of both oxidative processes is maintained at all scan rates with both features originating from a diffusion-controlled one-electron process. This is verified by the scan rate (ν) dependence of the peak current which gives a linear i_p *vs.* $\sqrt{\nu}$ plot for both oxidative processes (Fig. S2†). The solubility of **1** in MeCN is low and insufficient for spectroelectrochemical (IR-SEC) studies (see later), while **2** is completely insoluble in MeCN. We thus also carried CVs of **1** in CH_2Cl_2 (Fig. S3†) as **1** and **2** show good solubility in this solvent. At 0.1 V s^{-1} three irreversible oxidations are seen at E_p = +0.63 V, E_p = +1.16 V and E_p = +1.42 V and there is also an irreversible reduction at E_p = −1.91 V, with a shoulder at E_p = −1.72 V, the latter becoming prominent when the positive potential window is scanned first. The first oxidation shows reversibility when the potential is cycled below +1.30 V and it becomes fully chemically reversible ($i_{pa}/i_{pc} \sim 1$) when the potential is cycled below +1 V. The enhanced reversibility of the oxidations in MeCN *vs.* CH_2Cl_2 probably represents some solvent coordination with the generated cationic centres.

CVs of the edt-complex **3** (in MeCN) are also quite different from those of **1**. Thus, while **1** shows two reductive features, **3** shows only one. However, the most significant difference is that while the first oxidation of **1** is completely chemically reversible, the process in **3** is irreversible at all scan rates, showing only slight reversibility at higher scan rates when the CV is cycled between −0.8 V and 0.3 V (Fig. 6). Thus, the nature of the dithiolate bridge significantly alters the stability of the oxidised products. The more flexible pdt-bridge allows full reversibility of electron loss from the Fe_2 centre, while in contrast the more rigid edt renders the initially oxidised species unstable, possibly resulting from Fe–S bond scission.

CVs of **2** were recorded in CH_2Cl_2 and decamethylferrocene was used as an internal reference, however, for ease of comparison with **1**, data are reported *vs.* ferrocene (Fig. 7). Electrode passivation was a problem, and reproducible CVs were obtained only when the (glassy carbon) electrode was polished between each scan. At room temperature, **2** shows two quasi-reversible oxidations at $E_{1/2}$ = −0.11 V (ΔE = 540 mV) and $E_{1/2}$ = +0.66 V (ΔE = 260 mV) and a further irreversible oxidation at E_{an} = +1.05 V *vs.* $Fc^{+/0}$. Reversibility of the first oxidation is only maintained at faster scan rates, where i_{ca}/i_{an} reaches 0.95. As expected, oxidations of **2** occur at more negative potentials than those of **1** due to the increased electron-donating ability of dcpf *vs.* dppf. The first oxidation of **2** was studied at different scan rates and when normalised for scan rate, slower scan rates resulted in comparably higher currents. This may indicate a geometric rearrangement occurring on the same timeframe as the CV measurement resulting in potential inversion, *i.e.*, the potential of the second oxidation is lower than the first oxidation. We suggest that oxidation of **2** affords cation $[2]^+$, which undergoes a significant geometric rearrangement to give $[2^*]^+$. The oxidation potential of the latter is lower than that for the formation of $[2]^+$, leading to a spontaneous second oxidation occurring to give $[2^*]^{2+}$. In this scenario, while DFT calculations predict the lower energy mono-cation, $[2^*]^+$ over cation $[2]^+$, the former will not be observed spectroscopically.

CVs of **4a–c** (in MeCN) are different to **1** but similar to **3**. We present data for **4a** at scan rates ranging from 0.1–1.0 V s^{-1} (Fig. 8) and note that **4b** shows almost identical behaviour. Oxidation occurs at +0.13 V but shows no signs of any reversibility, while a second oxidation at +0.78 V shows some reversibility at all scan rates (ΔE = 110 mV). We suggest the first

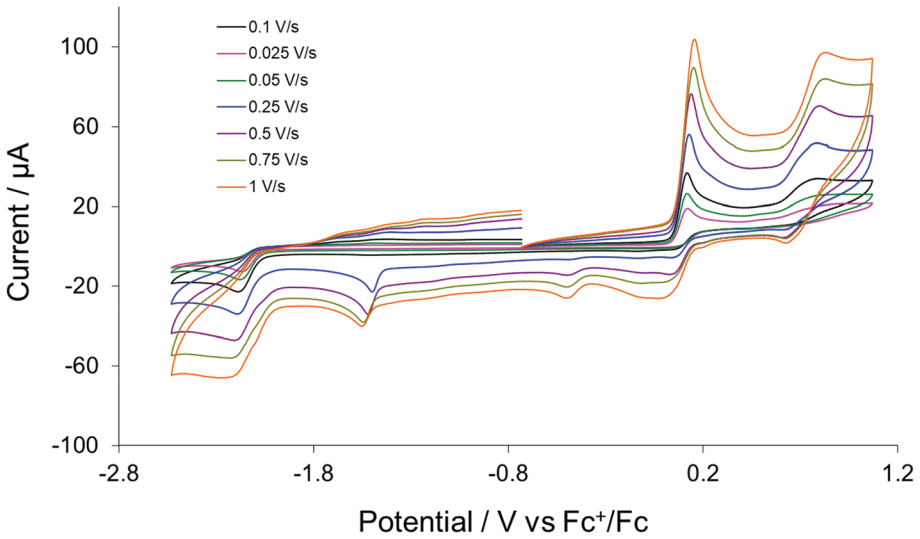

Fig. 6 CVs of **3** at various scan rates in MeCN (1 mM solution, supporting electrolyte $[NBu_4][PF_6]$, glassy carbon electrode, potential *vs.* Fc^+/Fc) scanning positive potential first.

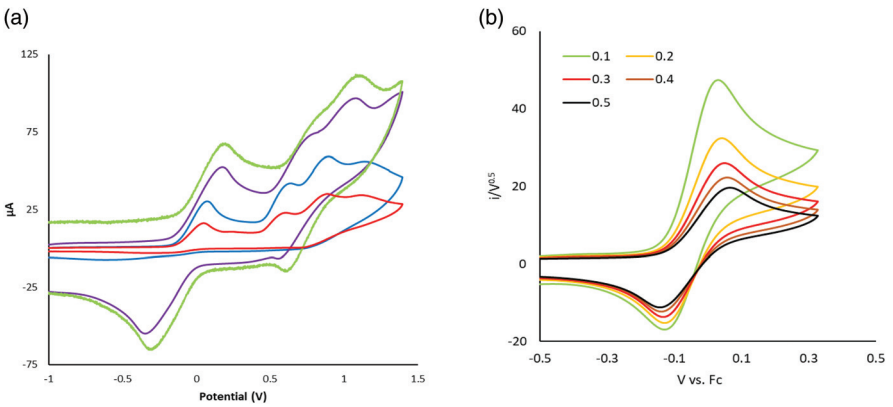

Fig. 7 CVs of **2** in CH_2Cl_2 at various scan rates (1 mM solution, supporting electrolyte $[NBu_4][PF_6]$, glassy carbon electrode, potential *vs.* Fc^+/Fc) scanning positive potential first (a) full scan, (b) first oxidation process.

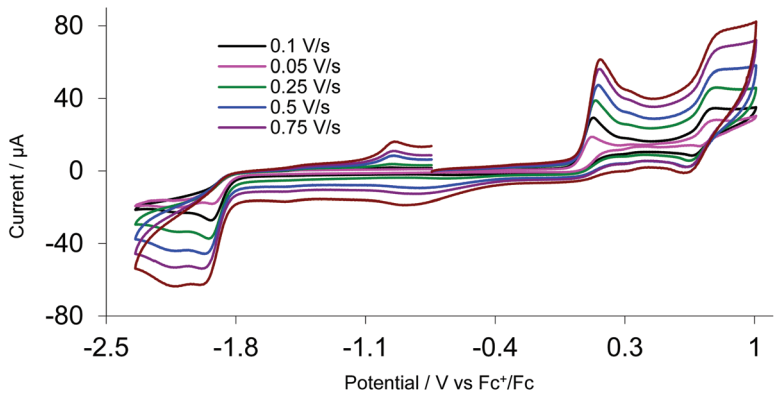

Fig. 8 CVs of **4a** MeCN at various scan rates (1 mM solution, supporting electrolyte $[NBu_4][PF_6]$, glassy carbon electrode, potential *vs.* Fc^+/Fc) scanning positive potential first.

process is an irreversible oxidation of the Fe_2 centre, and the second the quasi-reversible oxidation of the ferrocene. CVs for amino-functionalised **4c** were different (Fig. S4†), showing three separate oxidations at +0.04, +0.52 and +0.84 V, all of which are irreversible at all scan rates. The extra peak at +0.52 V is possibly due to the irreversible oxidation of the amino groups. Given the irreversible nature of the first oxidation process we did not further explore the oxidation chemistry of these bis(thiolate)-bridged complexes.

IR-spectroelectrochemistry (IR-SEC) of 1 and 2

Oxidation of [FeFe]-H_2ase biomimics results in a significant reduction in back-bonding, leading to a *ca.* 60 cm^{-1} hypsochromic shift in the highest frequency ν(CO) band,[29] while oxidation of a ferrocene centre separated by a heteroatom from the diiron centre results in a *ca.* 15 cm^{-1} hypsochromic shift.[30] In the event that oxidation results in a $\Delta\nu$(CO) that deviates significantly from these values, it is likely that some level of non-innocent behaviour is occurring. An important consideration when comparing CV and IR-SEC measurements is the timeframe of these experiments. The CV timeframe is significantly shorter than for the IR-SEC experiments, and the generated species are often different.

We first consider **2**, the results of which are concentration dependent (Fig. 9–11). Oxidation of a 3 mM solution results in initial formation of a new species characterised by a *ca.* +55 cm^{-1} hypsochromic shift of the ν(CO) bands being associated with formation of $[2]^+$, and subsequently a small amount of this cation transforms to $[2^*]^{2+}$ (see later) accompanied by an additional *ca.* 18 cm^{-1} shift (Fig. 9). IR data for $[2]^+$ is consistent with oxidation at the diiron centre, while the smaller second shift is consistent with oxidation at the ferrocenyl moiety. Together with our observation (above) that oxidation of **2** can result in potential inversion, this suggests that $[2^*]^{2+}$ is likely a dication, with one oxidation localised at the diiron centre, and the second at the ferrocenyl moiety.

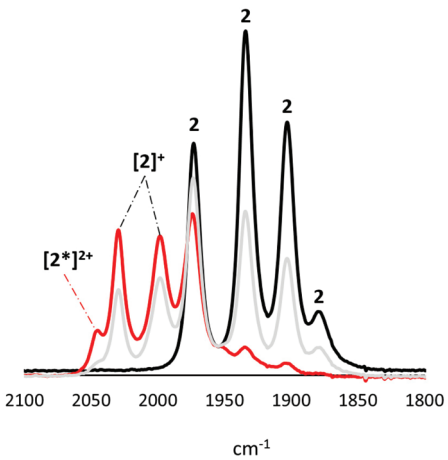

Fig. 9 IR-SEC for oxidation of **2** (black) (3 mM) in CH_2Cl_2 at RT. Grey scan shows neutral and oxidised species during oxidation, and red shows two species after full conversion of **2**.

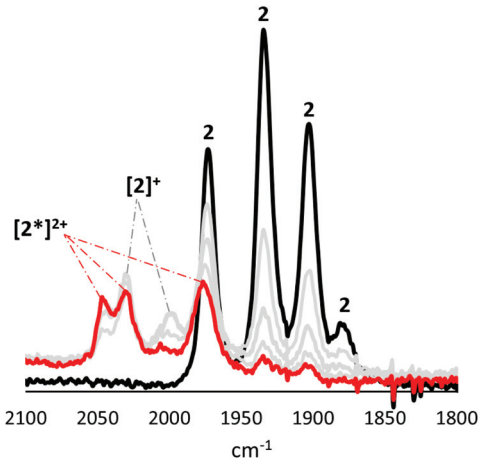

Fig. 10 IR-SEC showing oxidation of **2** (black) (0.5 mM) in CH_2Cl_2 at RT. Oxidation to give $[2^*]^{2+}$ is in red. In grey are intermediate scans showing conversion of **2** to $[2^*]^{2+}$ and the intermediate presence of $[2]^+$.

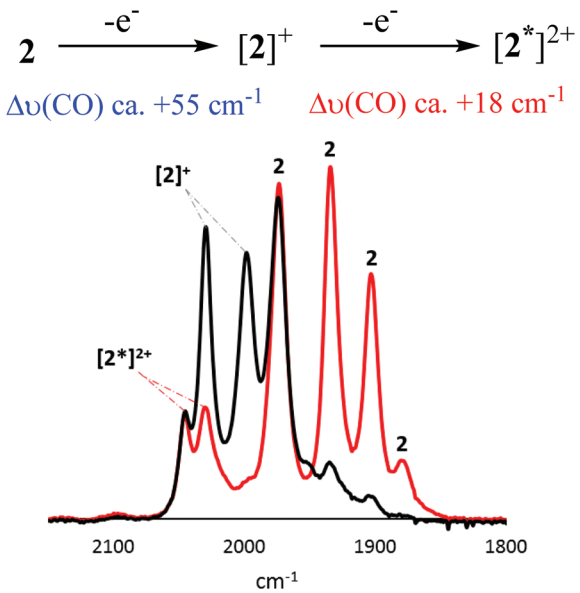

Fig. 11 IR-SEC of $[2]^+$ (black) in CH_2Cl_2 at RT and its reduction to **2** leaving $[2^*]^{2+}$ in solution (red).

Oxidation of a (less concentrated) 0.5 mM CH_2Cl_2 solution of **2** results in the near exclusive formation of $[2^*]^{2+}$ (Fig. 10). The apparent increased stability of $[2]^{2+}$ at this concentration may due to disproportionation of $[2]^+$. Furthermore, while $[2]^+$ can be reduced back to **2**, the product of the secondary transformation, $[2^*]^{2+}$, cannot be reduced to **2**. Neither $[2]^+$ nor $[2^*]^{2+}$ undergoes any further oxidative processes.

To better characterise $[2]^+$, we carried out oxidation of **2** at 253 K in PrCN (Fig. 12). Under these conditions exclusive formation of $[2]^+$ results, with no evidence of formation of $[2^*]^{2+}$, possibly since the activation energy for the structural rearrangement leading to potential inversion is now too high. Rather, scanning to higher potentials generates a dication,

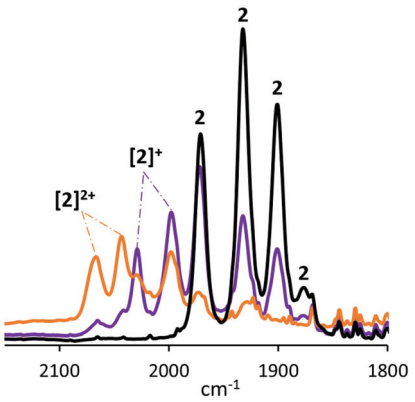

Fig. 12 IR-SEC of **2** (1 mM) in PrCN at 253 K showing first (purple) and second oxidation (orange) of a solution of **2** (black).

accompanied by a $\Delta\nu$(CO) of *ca.* +39 cm^{-1} shift, a value that does not fit hypsochromic shifts expected for localised oxidations at either diiron or ferrocenyl centres, and might be explained either by a second oxidation delocalised over the whole molecule, or by oxidation at the diiron centre followed by solvent coordination. Given the instability of $[\mathbf{2}]^+$ and DFT calculations (see later) which suggest the presence of a μ-CO in the cation (and thus a vacant coordination site) it seems most plausible that solvent binding to give $[\mathbf{2}(PrCN)]^{2+}$.

As summarised (Fig. 13) CV and IR-SEC reveal that **2** undergoes a diiron-based oxidation at E_{an} = −0.10 V in CH_2Cl_2 to give $[\mathbf{2}]^+$. This cation is relatively unstable and undergoes a significant structural rearrangement to another species, $[\mathbf{2}^*]^+$, which permits a ferrocene-based oxidation at a potential lower than −0.10 V (potential inversion). This event in turn yields the (triplet) dication, $[\mathbf{2}^*]^{2+}$, in which one "hole" is localised on the diiron centre and the second at ferrocene. Although the (singlet) dication, $[\mathbf{2}]^{2+}$, is not observed spectroscopically, under the different time scales and reaction conditions of CV, formation of this species may be responsible for the oxidative wave at E_{an} = +0.66 V.

We next turn our attention to SEC of **1**, all experiments being performed in CH_2Cl_2. At room temperature, the behaviour of **1** is similar to **2**. Oxidation of a 1 mM (or more concentrated) solution of $[\mathbf{1}]$ to $[\mathbf{1}]^+$ initially results in a hypsochromic shift of *ca.* +60 cm^{-1} (Fig. 14(i)). This transformation can also be affected chemically upon addition of $[Cp_2Fe][PF_6]$ to CH_2Cl_2 solutions of **1**. In the SEC experiment, the presence of a shoulder at 2056 cm^{-1} (red trace) and the larger than otherwise expected absorption at 1983 cm^{-1}, is attributed on the basis of the chemistry of **2**, to formation of $[\mathbf{1}^*]^{2+}$. Unfortunately, overlap of the absorptions prohibited acquisition of information regarding ratios of the two species, and passivation of the electrode over time prevented further studies into the conversion of $[\mathbf{1}]^+$ to $[\mathbf{1}^*]^{2+}$. Scanning $[\mathbf{1}]^+$ to higher potentials results in a second oxidation which, due to electrode passivation, is not well-resolved (Fig. 14(ii)). Nevertheless, a shift in the highest frequency ν(CO) band by *ca.* +60 cm^{-1} indicates that a second diiron-based oxidation seems likely and may correspond to formation of $[\mathbf{1}]^{2+}$.

Previously reported electrocatalytic H_2 oxidation studies with **1** were conducted in MeCN.[8] The activation barrier to the rearrangement of $[\mathbf{1}]^+$ and $[\mathbf{2}]^+$, which permits formation of $[\mathbf{1}^*]^{2+}$ and $[\mathbf{2}^*]^{2+}$ respectively, may be significantly different in the presence of a coordinating solvent. Unfortunately, due to the low solubility of **1** and **2** in MeCN leading to immediate complex adsorption onto the electrode, all attempts to record IR SEC in this solvent were unsuccessful. The lower solubility of **1** *vs.* **2** in CH_2Cl_2 also hampered our attempts to study SEC at low temperature. Only weak and broad new IR bands were

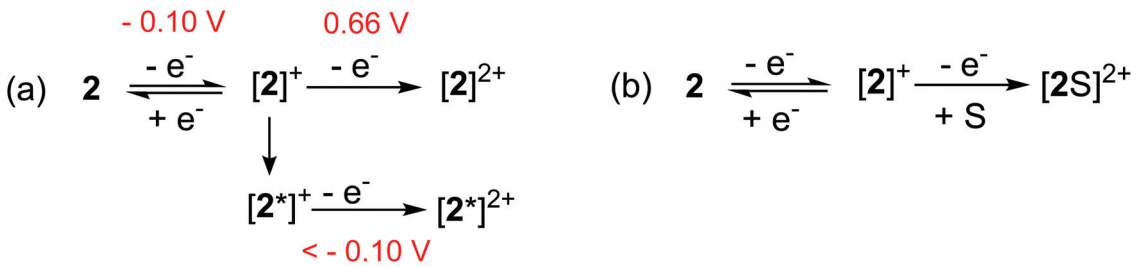

Species	ν(CO) / cm^{-1}
2	1972, 1934, 1903, 1879
$[\mathbf{2}]^+$	2027, 1997, 1973
$[\mathbf{2}^*]^{2+}$	2045, 2028, 1977
$[\mathbf{2}]^{2+}$	2066, 2042

Fig. 13 Proposed oxidation-induced chemistry of **2** in (a) CH_2Cl_2, and (b) PrCN (S) with a table giving ν(CO) absorptions.

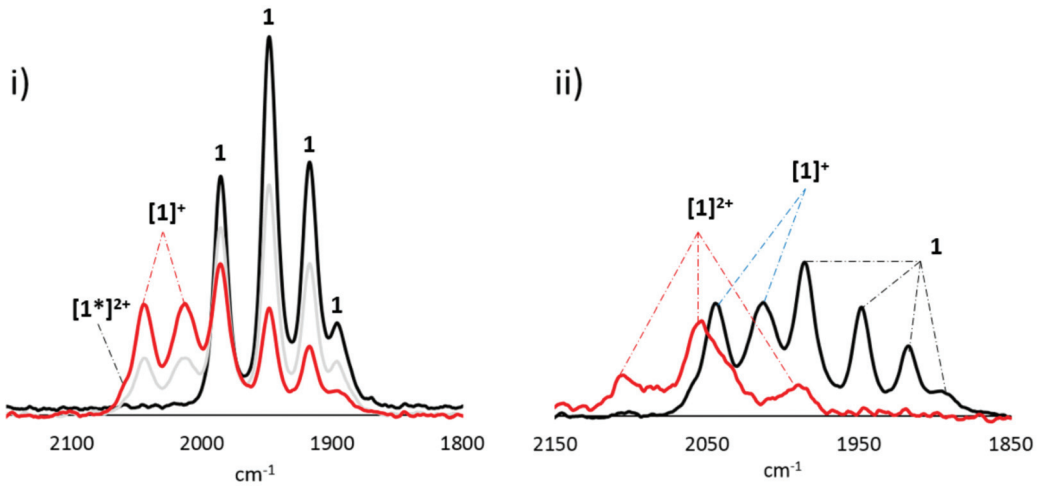

Fig. 14 IR-SEC of **1** (1 mM) in 0.1 M $[Bu_4N][PF_6]/CH_2Cl_2$ showing (i) first oxidation and (ii) second oxidation. Red trace shows most oxidised species.

observed which afforded little insight. We thus turned to DFT calculations (see below) for further clarification of the nature of the cations formed upon oxidation and to identify which species is/are responsible for the catalytic activity seen in MeCN.

DFT calculations on oxidised forms of $Fe_2(CO)_4(\mu\text{-pdt})(Me_2PC_5H_4FeC_5H_4PMe_2)$ (A)

In order to better understand the nature of the oxidised species formed in experiments described above, we have carried out DFT calculations on oxidised forms of $Fe_2(CO)_4(\mu\text{-pdt})(Me_2PC_5H_4FeC_5H_4PMe_2)$ (**A**), namely the radical cation **B** and triplet (^{3}**C**) and singlet (^{1}**C**) electronic configurations of dication **C** (Fig. 15). One electron oxidation of **A** results in a significant change to the geometry, resulting in formation of a semi-bridging carbonyl *via* a pronounced trigonal twist of one $Fe(CO)_2P$ centre leading to a significant lengthening of the Fe–Fe vector to 2.645 Å. Clearly a significant reduction of electron-density between the diiron centres results from this oxidation, suggesting that the hole is localised between these sites. The spin density plot of **B** (Fig. 16) confirms the Fe–Fe bond as the site of the first oxidation. Interestingly, we see no evidence of a semi-bridging carbonyl in the SEC of either **1** or **2**. This suggests that there may be a significant activation energy for the trigonal twist of the $Fe(CO)_2P$ centre and thus in oxidation catalysis the ground state conformation **B** of the mono-cation may not be accessible.

The HOMO of radical cation **B** is largely based on the ferrocene, suggesting that the second oxidation would lead to electron loss from this centre. In support of this, we find that the most stable form of dication **C** is the triplet form ^{3}**C** which has a highly rotated structure, being *ca.* 17.5 kcal mol^{-1} more stable than the singlet form. While this manuscript was in preparation, De Gioia, Zampella and co-workers reported related calculations on $[\mathbf{1}]^{2+}$ (phenyl groups included) and came to (broadly) similar conclusions.[31] The energy order of singlet and triplet states was functional-dependent; with B3LYP functional the ground state is the triplet form, while with BP86, triplet and singlet states are nearly degenerate.[31] This suggests that electron transfer from the Fe_2 to Fc centres, resulting in conversion of ^{3}**C** to ^{1}**C**, may be facile, and this may go some way to explain the two spectroscopically identified

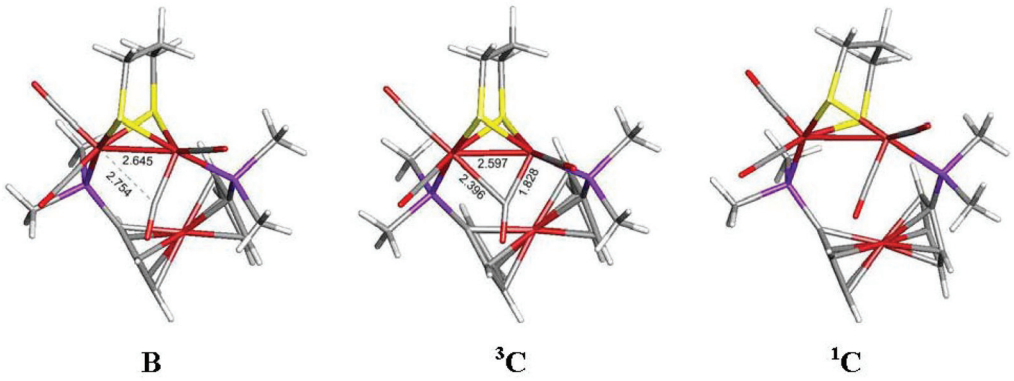

Fig. 15 Radical cation **B**, and triplet (^{3}**C**) and singlet (^{1}**C**) electronic configurations of the dication **C**.

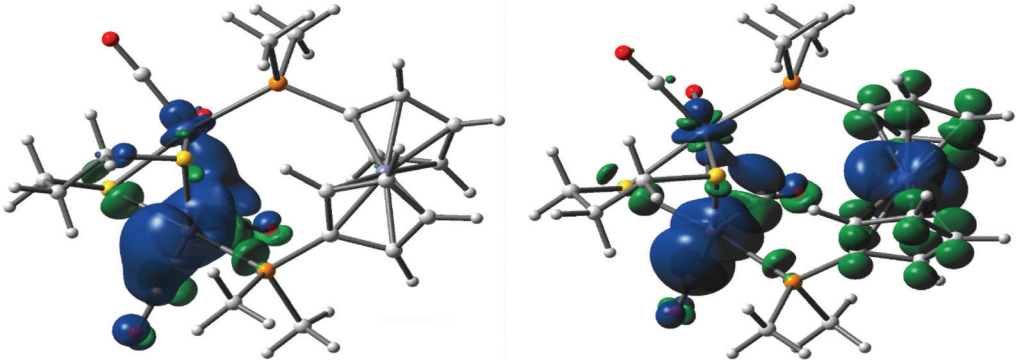

Fig. 16 Spin density plots of the radical cation **B** (left) and the triplet dication ^{3}**C** (right). The isovalue for each α-spin based contour plot is 0.02.

dications. The spin density in ^{3}**C** is largely delocalised over the three iron centres (Fig. 16) with smaller contributions for the Cp rings and the CO ligands. Cations $[\mathbf{1}]^{2+}$ and $[\mathbf{2}]^{2+}$ have a doubly oxidised diiron centre and likely correspond to the ^{1}**C** dication configuration, while $[\mathbf{1}^*]^{2+}$ and $[\mathbf{2}^*]^{2+}$ would correspond to the ^{3}**C** configuration. This also correlates to the observed preferential formation of the lower energy ^{3}**C** configurations, $[\mathbf{1}^*]^{2+}$ and $[\mathbf{2}^*]^{2+}$, if the system has sufficient energy (298 K). Energy barriers to the formation of ^{3}**C** and ^{1}**C** have not been calculated, and intermolecular or solvent effects on the stability of these species (or indeed their intermediates) have not been considered. However, that formation of $[\mathbf{1}]^{2+}$ and $[\mathbf{2}]^{2+}$ occurs at low temperatures (253 K) suggests that formation of the more stable ^{3}**C** configuration involves a large energy barrier. It is worth noting that we observe no conversion of $[\mathbf{1}]^{2+}$ and $[\mathbf{2}]^{2+}$ to their respective lower energy states $[\mathbf{1}^*]^{2+}$ and $[\mathbf{2}^*]^{2+}$.

Protonation of 1 and 2

Chelate complexes $Fe_2(CO)_4(\kappa^2$-diphosphine)(μ-dithiolate) protonate readily to afford stable hydride-bridged cations, $[Fe_2(CO)_4(\mu\text{-H})(\kappa^2$-diphosphine)(μ-dithiolate)$]^+$,[13,20,27,32] while in contrast related (sometimes isomeric) species with a bridging diphosphine are protonated only slowly by strong acids and (generally) form unstable cations.[18] There are two exceptions to this chelate *vs.* bridge behaviour, namely bridging complexes with highly basic diiron centres or those with very flexible diphosphines. For example, protonation of $Fe_2(CO)_4(\mu$-$Cy_2PCH_2PCy_2)$(μ-pdt) by $HBF_4{\cdot}Et_2O$ readily affords crystallographically characterised $[Fe_2(CO)_4(\mu\text{-H})(\mu\text{-}Cy_2PCH_2PCy_2)(\mu\text{-pdt})][BF_4]$,[18] while in contrast $Fe_2(CO)_4(\mu\text{-}Ph_2PCH_2PPh_2)$(μ-pdt) protonates only upon addition of excess $HBF_4{\cdot}Et_2O$ and the resulting cation shows limited stability.[18,33] A second example relates to $Fe_2(CO)_4\{\mu\text{-}Ph_2P(CH_2)_4PPh_2\}$(μ-pdt), which, unlike related species with fewer methylene groups in the backbone, reacts with $HBF_4{\cdot}Et_2O$ to form a relatively stable cationic hydride [**20**]. The reason(s) for the different protonation behaviour of $Fe_2(CO)_4\{\mu\text{-}Ph_2P(CH_2)_4PPh_2\}$(μ-pdt) are less clear, as the diiron centre appears to have similar basicity to other diphosphine-bridged analogues. We have previously attributed this behaviour to the more flexible nature of this diphosphine, as shown by the relatively elongated iron–iron bond.

Given the elongated nature of the iron–iron bond in **1**, this seemed to be a good opportunity to test this hypothesis. Addition of a slight excess of $HBF_4{\cdot}Et_2O$ to a CH_2Cl_2 solution of **1** resulted in the rapid formation of $[Fe_2(CO)_4(\mu\text{-H})(\mu\text{-dppf})(\mu\text{-pdt})][BF_4]$, [**1H**][$BF_4$] (Scheme 3). Interestingly, unlike related cationic-chelate complexes which generally do not easily deprotonate, addition of pyridine to $\mathbf{1H}^+$ leads to regeneration of **1**. Characterisation of $\mathbf{1H}^+$ was straightforward, bands at 2058s, 2040s, 2002s cm^{-1} in the IR spectrum being shifted *ca.* +72–91 cm^{-1} to lower frequencies consistent with removal of significant electron-density from the diiron centre. The ^{31}P $\{^1H\}$ NMR spectrum shows a singlet at 44.8 ppm, consistent with a bridging hydride and this is confirmed by the obser-

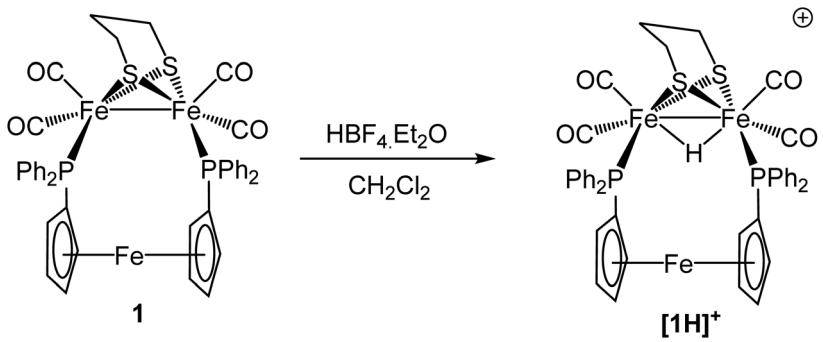

Scheme 3 Protonation of **1** to afford $[\mathbf{1H}]^+$.

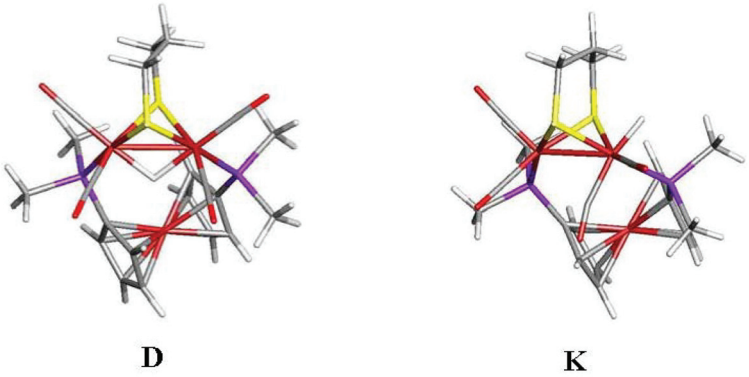

Fig. 17 Calculated molecular structures for isomers of $1H^+$ with bridging (D) and terminal (K) hydrides.

vation of a triplet at δ −12.40 (J_{PH} 17.6 Hz) in the ^{1}H NMR spectrum.

We have been unable to grow crystals of $\mathbf{1H^+}$ suitable for X-ray analysis. Thus, we used DFT theory to calculate its ground state structure **D** and compare it with an isomer **K** with a terminal hydride (Fig. 17) finding that the former is *ca.* 22.4 kcal mol^{-1} lower in energy than the terminal hydride **K**. An Fe–Fe bond length of 2.642 Å is calculated for **D** suggesting that little overall structural rearrangement occurs to **1** upon protonation.

Protonation of **2** with $HBF_4{\cdot}Et_2O$ in CD_2Cl_2 similarly affords $[Fe_2(CO)_4(\mu\text{-H})(\mu\text{-dcpf})(\mu\text{-pdt})][BF_4]$, $[\mathbf{2H}][BF_4]$. In the IR spectrum, peaks are moved to higher wavenumbers, and that at highest frequency is shifted by 82 cm^{-1}. The spectral pattern is, however, a little different from that of $\mathbf{1H^+}$, the lowest energy peak in $\mathbf{2H^+}$ appearing at 1975 cm^{-1}, as opposed to 2002 cm^{-1} in $\mathbf{1H^+}$. We are not sure why this difference occurs. It may suggest a greater asymmetry in the molecule, as the low energy vibration is less shifted than might be expected. Both the hydride signal in the ^{1}H NMR spectrum at δ −13.4, and the singlet in the $^{31}P\{^1H\}$ NMR spectrum at 53.3 ppm are broad, which may be due to a fluxional process or contamination by paramagnetic $\mathbf{2^+}$, since oxidation of **2** is so facile (see below). Unlike $\mathbf{1H^+}$, addition of pyridine to $\mathbf{2H^+}$ did not result in the regeneration of **2**, suggesting (as might be expected) that the hydride is more tightly bound than in $\mathbf{2H^+}$.

Catalytic proton-reduction

Catalytic proton-reduction (the hydrogen evolution reaction) by [FeFe]-ase biomimics has been widely studied,[34] We previously communicated that **1** catalyses proton-reduction in MeCN with $HBF_4{\cdot}Et_2O$ as the proton source.[8] Fig. 18 shows CVs upon addition of 1–10 equivalents of the acid. A new reduction wave appears at *ca.* −1.7 V which we associate with

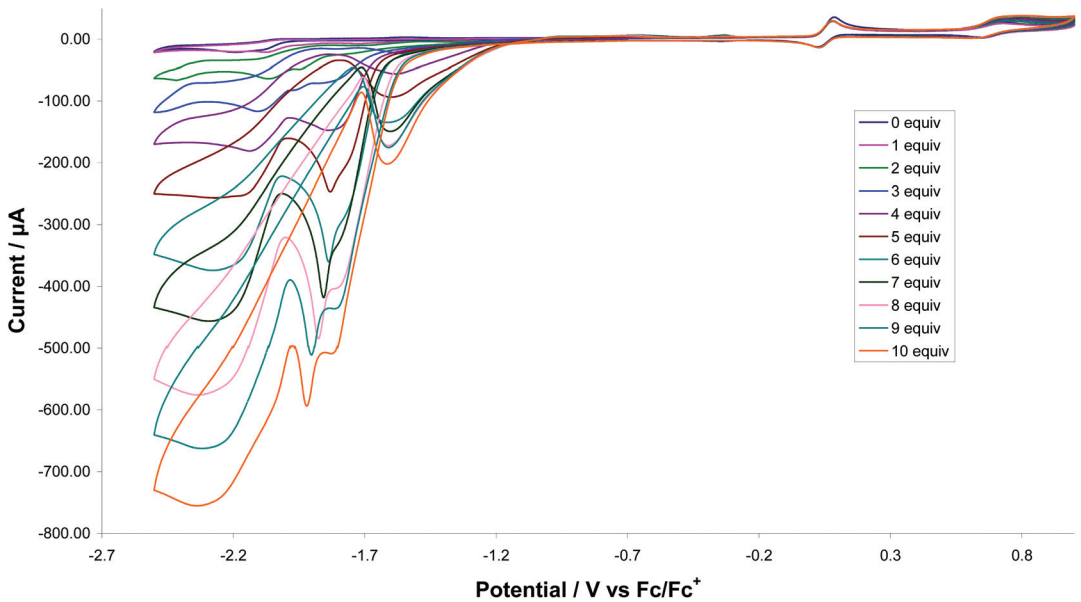

Fig. 18 CVs of **1** in the absence of acid and in the presence of up to 10 molar equivalents of HBF_4 (1 mM solution in acetonitrile, supporting electrolyte $[NBu_4][PF_6]$, scan rate 0.1 V s^{-1}, glassy carbon electrode, potential *vs.* Fc^+/Fc).

hydride-bridged cation $\mathbf{2H}^+$ and this was confirmed in an independent experiment. The height of this peak grows with increasing acid addition consistent with proton-reduction and with higher amounts of acid (>7 equivalents) it splits into two distinct waves. The nature of the second of these (at *ca.* −1.8 V) is not known but could be associated with a terminal hydride species akin to **K**. A second catalytic wave is also observed at *ca.* −2.10 V which competes with the direct reduction of the acid at the glassy carbon electrode (>2.0 V).[35] On the return scan a further reductive wave is seen at −1.55 V which also increases with acid concentration implying that a sufficiently stable species is generated in the depletion layer during catalysis on the forward scan which can release H_2 by reducing at this potential.[36] Thus it appears that **1** enters into the catalytic cycle *via* a CE mechanism to generate the neutral paramagnetic complex $[Fe_2(CO)_4(\mu\text{-H})(\mu\text{-dppf})(\mu\text{-pdt})]$ (**1H**) upon reduction of $\mathbf{1H}^+$, which can then either further protonate or undergo reduction. Peak heights of the oxidative process do not change during the experiment showing the robustness of **1** under the catalytic operating conditions.

Proton-reduction studies of **2** were carried out in CH_2Cl_2, using CF_3CO_2H as a proton source, but under these conditions poor catalytic activity resulted (Fig. S5†). After addition of 3 equivalents of the acid, while it is clear from changes in the oxidation chemistry that **2** is no longer the major species in solution, somewhat surprisingly there is still no reductive chemistry visible within the potential window. After addition of 7 acid equivalents further changes are seen to the oxidation chemistry and a new reductive process is observed at *ca.* −1 V, but the extremely broad nature suggests that a single stable species is not generated. After 15 acid equivalents the oxidation chemistry again changes with a relatively sharp reductive process being seen at *ca.* −1.2 V. It is difficult to interpret these data and we will not speculate too much, apart from suggesting that perhaps at high acid concentrations (*ca.* 15 equivalents) a bis(hydride) dication $[\mathbf{2HH}]^{2+}$ results, which has a reduction potential within the spectral window.

Somewhat surprisingly, given the irreversible nature its first reduction potential, edt-analogue **3** shows similar catalytic behaviour to **1** with respect to electrocatalytic proton reduction. This provides further evidence that protonation occurs prior to reduction and presumably $[\mathbf{1H}]^+$ and $[\mathbf{3H}]^+$ have similar reduction potentials.

DFT studies probing the mechanism of catalytic proton-reduction by 1

In order to better understand the proton-reduction behaviour of **1** we have carried out a series of DFT calculations based on $Fe_2(CO)_4(\mu\text{-pdt})(Me_2PC_5H_4FeC_5H_4PMe_2)$ (**A**) which allow an overall reaction scheme to be postulated (Scheme 4).

As established from the experimental studies, protonation affords cation **D**. This is not basic enough to add a second proton but reduces to afford the neutral 35-electron complex **E** (Fig. 19a). A small number of related 35-electron species including $Fe_2(CO)_4(\mu\text{-H})(PMe_3)_2(\mu\text{-pdt})$[37] and $Fe_2(CO)_2(\kappa^2\text{-dppv})_2(\mu\text{-H})(\mu\text{-pdt})$[38] have been prepared and both experimental data and DFT studies suggest symmetrically bridging hydrides. Somewhat unexpectedly then, our DFT calculations for **E** suggest that upon reduction the hydride binds in an unsymmetrical manner to the diiron centre, with Fe–H distances of 1.973 and 1.577 Å. Zampella and co-workers have carried out DFT calculations on a range of cationic 34-electron diiron dithiolate complexes with both terminal (t-H) and bridging (μ-H) hydrides and their one-electron reduced products which has allowed some useful insights.[39] While most μ-H cations reduce to give 35-electron species in which the hydride remains in this position, in one case the reduced product is calculated to be a t-H with a significantly elongated the Fe–Fe vector. Thus, while the semi-bridging nature of the hydride in **E** is unexpected it is not unprecedented. It is also shown that,

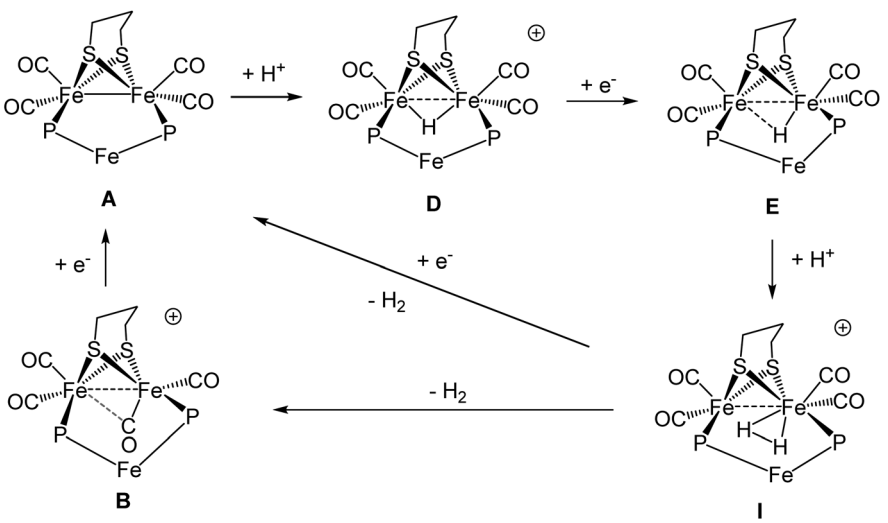

Scheme 4 Proposed reaction pathway for proton-reduction catalysed by **1**.

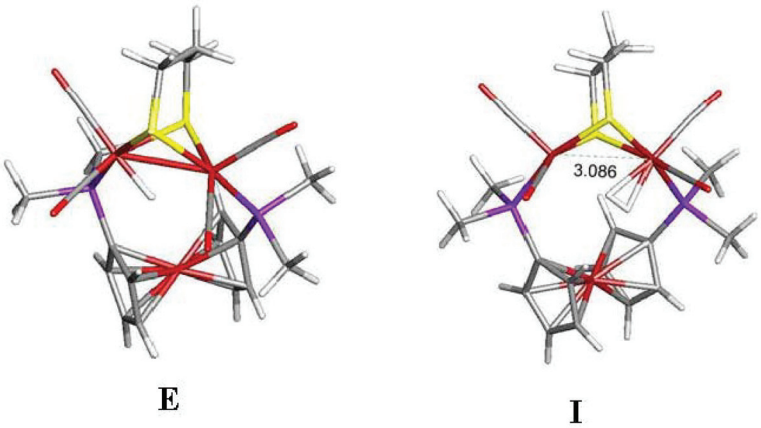

Fig. 19 Calculated molecular structures for 35-electron species (a) **E** and (b) **I**.

while in μ-H complexes the spin density is delocalised across the Fe_2 centre, in t-H analogues it is localised at the non-hydride bound iron atom, and thus such species are best considered as Fe(I)–Fe(II) mixed-valence complexes.[39] Finally, the reduction potential of 35-electron radicals is very sensitive to the coordination nature of the hydride with t-H species reducing at consistently lower potentials than their μ-H analogues. Thus, while the structure of **E** is unexpected, it is also highly beneficial with respect to proton-reduction behaviour.

As discussed in the previous section, **E** is a potential branching point, as it can be either protonated or further reduced. DFT calculations suggest that protonation leads to the mixed-valence dihydrogen complex **I** (Fig. 19b) in which H_2 is bound to an Fe(II) centre, which also results in a further elongation of the Fe–Fe vector from 2.869 Å (in **E**) to 3.086 Å. Loss of H_2 from **I** affords radical cation **B** or **I** can be reduced further, regenerating **A** upon H_2 loss. As the reduction potential for t-H complexes are lower than those for μ-H analogues, we cannot discount possible reduction of **E** to generate 36-electron anion **F**. This is calculated to have a t-H and no direct Fe···Fe interaction (Fig. S6†).

H_2 binding studies

Catalytic H_2 oxidation by [FeFe]-ase biomimics remains a significant challenge with few authenticated examples of H_2 activation.[7,8,40] In the enzymes, the active catalytic H_2 oxidation site (H_{ox}) is a mixed-valence Fe(II)–Fe(I) state.[41] Recent theoretical work by De Gioia, Zampella and co-workers has attempted to rationalise the ideal conditions needed for H_2 oxidation[31,41] (see discussion below). Their findings include: the mixed-valence diiron centre should not be too basic for H_2 binding to be favorable and the presence of the Fe_4S_4 cluster (or surrogate) is essential as it allows electron delocalisation upon H_2 binding.[31] Molecular hydrogen oxidation is a two-electron process and we reasoned that the ability to access $[\mathbf{1}]^{2+}$ electrochemically (in MeCN) containing a mixed-valence Fe_2 core that is not too electron-rich, and an oxidised dppf moiety, which can act as a surrogate of the Fe_4S_4 cluster, may provide a favorable centre for H_2 oxidation.

We first tried to detect H_2 binding to oxidised forms of **1** and **2** electrochemically but CVs of **1** in MeCN in the absence and presence of H_2 showed little change (Fig. S7†). We next turned to IR spectroscopy, generating oxidised forms of **1** and **2** in CH_2Cl_2 upon addition of an excess of the thianthrene (TA) radical cation, [TA][PF_6]. For **2**, on the basis of the IR spectrum (Fig. S8†), oxidation produces both $[\mathbf{2}]^+$ and $[\mathbf{2}^*]^{2+}$, while for **1**, it appears that $[\mathbf{1}]^+$ primarily results, however, due to overlap of IR signals for $[\mathbf{1}]^+$ and $[\mathbf{1}^*]^{2+}$, the presence of small amounts of $[\mathbf{1}^*]^{2+}$ cannot be excluded. H_2 was then bubbled through these solutions (5 min) and a second IR spectrum recorded. In both cases, small changes were seen following H_2 addition, but no compelling evidence for H_2 binding could be found. For **1**, a (very) small new absorption was seen at 2069 cm^{-1}. If dication $[\mathbf{1}^*]^{2+}$, at best present in small amounts, binds H_2 then we might expect to see only a small change in IR spectra.

We next used DFT calculations to probe the likely nature of H_2 binding and activation at the dication site. This has recently been independently addressed by De Gioia, Zampella and co-workers.[31] They found two possible binding sites for H_2 to ^{3}**C**, at the apical site of the rotated $Fe(CO)_2P$ moiety and at the diiron bond, the latter being favorable. We focused exclusively on H_2 binding to the apical site, which *via* a Kubas interaction (in which H_2 acts as both a donor and acceptor) results in formation of singlet **J** (Fig. 20). Thus, upon H_2 binding electron-transfer occurs leading to the effective formation of Fe(II)–Fe(II) diiron centre.

Catalytic H_2 oxidation

We previously communicated that **1** catalyses H_2 oxidation in the presence of pyridine which acts as an external base.[8] Thus, while we have been unable to access $[\mathbf{1}]^{2+}$ in significant amounts to fully probe H_2 binding, we can access it electrochemically. Upon addition of 1 equivalent of pyridine to **1** in MeCN, the oxidation wave at +0.05 V remains unchanged but the oxidative peak current of the second oxidation process, associated with generation of $[\mathbf{1}]^{2+}$ increased by *ca.* 10 mA, and upon sequential addition of up to 10 equivalents of pyridine

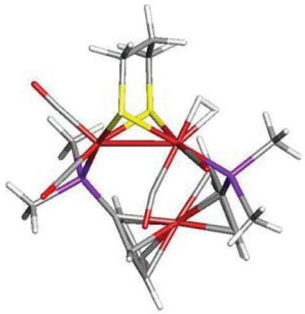

J

Fig. 20 Calculated structure of **J** generated from H_2 binding to **3C**.

the current increase was 22 mA (Fig. 21). No such catalytic wave was observed when the same experiment was carried out in absence of base. In contrast to the behaviour of **1**, the edt-analogue **3** does not oxidise dihydrogen suggesting that the reversibility of the first (diiron-based) oxidation is a requirement for this type of diiron complexes to act as an electrocatalyst for dihydrogen oxidation.

To probe a possible H_2 activation pathway we returned to DFT. As discussed above, H_2 binding to $[\mathbf{1}]^{2+}$ affords singlet **J** (Fig. 20) with diiron centre. Subsequent removal of H^+ (by an external base) affords the terminal hydride **K**, which is unstable with respect to the bridging isomer **D**, the same species being formed upon protonation of **A** (Scheme 5). Interestingly, De Gioia, Zampella and co-workers found a different H_2 activation pathway, whereby H_2 scission led to for-

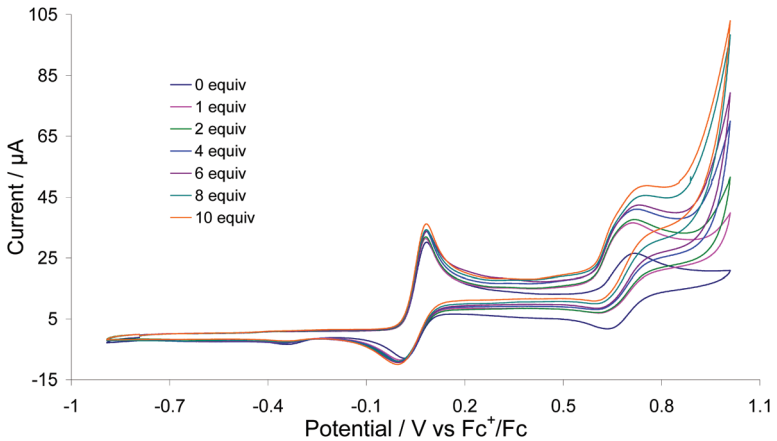

Fig. 21 CVs of **1** under a H_2 atmosphere in the absence of pyridine and in the presence of 1–10 molar equivalents (1 mM solution in MeCN, supporting electrolyte $[NBu_4][PF_6]$, scan rate 0.1 V s^{-1}, glassy carbon electrode, potential *vs.* Fc^+/Fc).

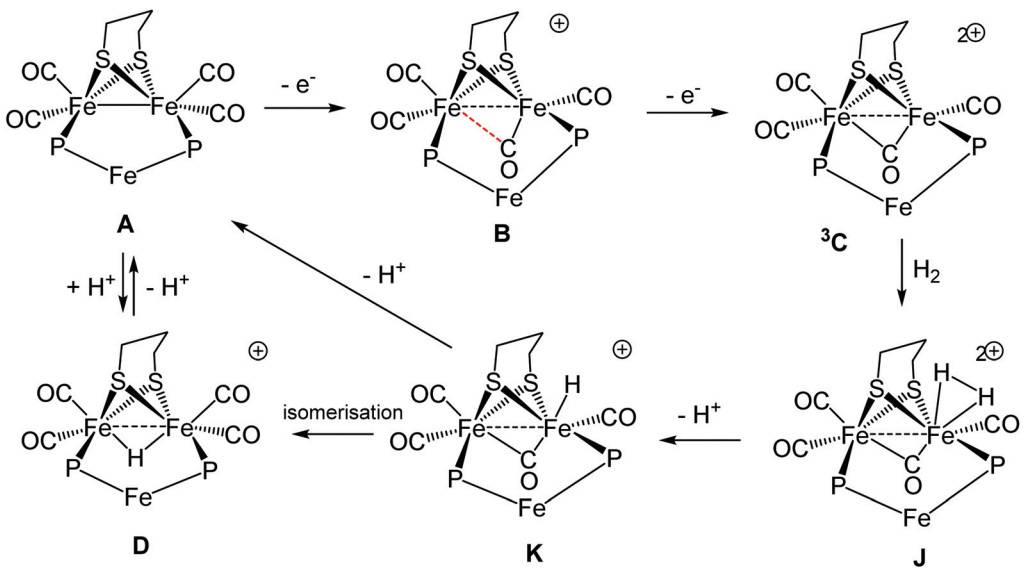

Scheme 5 Proposed reaction pathway(s) for the H_2 oxidation catalysis by **1**.

mation of a dihydride in which one proton bridged the diiron centre and the other at the ferrocene.[31] Thus, the dppf/dcpf ligands may be playing a role of both a redox and chemical centre, something that we had not previously considered. Presumably if this indeed occurs, then it is the ferrocene-bound hydride that is deprotonated by external base and thus the same cationic bridging hydride **D** results.

We can thus propose an overall reaction pathway for the H_2 oxidation catalysis by **1** based on these calculations (Scheme 5). Key steps are the formation of a triplet dication which is able to bind H_2 and (importantly) this binding leads to an increase in electron-density at the diiron centre which in turn favors electron-transfer to the Fe(III) ferrocenium site; the overall conversion of the Fe_2(I)/(II)–Fc(III) centre to an Fe_2H_2(II)/(II)–Fc(II) state. Abstraction of a proton from this complex results in formation of a cationic hydride, the most stable state of which is in the bridging site. $[Fe_2(CO)_4(\mu\text{-H})(\mu\text{-pdt})(\mu\text{-dppf})]^+$ (**1H$^+$**) results from the addition of strong acids to **1**, a reaction that is reversed in the presence of strong bases, thus closing the catalytic cycle. This is undoubtedly a key step, as oxidation of **1H$^+$** would occur only at high potentials and thus conversion of **1H$^+$** (**D**) to **2** (**A**) is likely to be rate-limiting.

Summary and conclusions

In this contribution we have prepared and characterised a small series of new [FeFe]-ase biomimics which contain a ferrocenyl diphosphine as a surrogate for the Fe_4S_4 moiety in the H-cluster of the enzyme. In all, the diphosphine bridges the diiron centre and this likely results from the thermodynamic stability of these species over the initially targeted chelate isomers. The two redox active centres are *ca.* 4.5–4.7 Å apart in the solid-state and the flexibility of the diphosphine should allow them to get slightly closer in solution, to be comparable with the average $Fe_4S_4\cdots Fe_{proximal}$ distance in the enzyme of *ca.* 4 Å.[42] To investigate cooperativity between the two redox centres, we carried out a series of CV experiments. While oxidation of the edt and SAr complexes was irreversible, the first oxidation of **1–2** showed (chemically) reversible or quasi-reversible character (in MeCN) and bathochromic shifts in IR-SEC (in CH_2Cl_2) allow us to correlate this with electron-loss from the Fe_2 centre, while the second oxidation likely results from the ferrocenyl centre. The nature of the oxidised species was further probed by DFT calculations which suggest that the experimental assignment of oxidation centres is correct, and the most stable form of the dication is a triplet state with a highly rotated structure. The quasi-reversibility of the second oxidation in the pdt complexes suggests that chemically the removal and addition of two electrons is reversible but it is difficult to say unambiguously whether the two oxidised centres interact directly. Nevertheless, the dppf complex is able to oxidise H_2 in the presence of added base at its second oxidation potential, although all others are inactive, being associated with the irreversible nature of the first oxidation. As H_2 oxidation is a two-electron process, at some point an electron must be transferred from (bound) H_2 to the Fe(III) ferrocenyl centre although it remains unclear as to when this occurs. All the ferrocenyl diphosphine complexes are also able to reduce protons to H_2, a process which occurs *via* initial protonation of the diiron centre, and thus $Fe_2(CO)_4(\mu\text{-dppf})(\mu\text{-pdt})$ is a true [FeFe]-ase biomimic in that it is able to catalyse the reaction in both directions.

Experimental

General procedures

All reactions were carried out using standard Schlenk-line techniques under N_2 and reaction solvents were purified on alumina columns. Work-up was done in air using standard bench reagents. Diiron hexacarbonyls were prepared by standard procedures[43–46] and diphosphines were purchased from Aldrich and used as supplied. NMR spectra were recorded on a Bruker AMX400 spectrometer and referenced internally to the residual solvent peak (^{1}H) or externally to $P(OMe)_3$ (^{31}P). Infrared spectra were recorded on a Nicolet 205 FT-IR spectrometer in a solution cell fitted with calcium fluoride plates, subtraction of the solvent absorptions being achieved by computation. Fast atom bombardment mass spectra were recorded on a VG ZAB-SE high resolution mass spectrometer and elemental analyses were performed at UCL.

Synthesis of $Fe_2(CO)_4(\mu\text{-dppf})(\mu\text{-pdt})$ (1). $Fe_2(CO)_6(\mu\text{-pdt})$ (0.10 g, 0.26 mmol) and dppf (0.14 g, 0.26 mmol) in toluene (100 ml) were heated at reflux for 5 d resulting in a colour change from orange to red-brown. After cooling to room temperature, volatiles were removed under reduced pressure to give a dark oily red residue. This was washed with hexanes (3 × 5 mL) and dried. Extraction into a minimum volume of CH_2Cl_2 followed by addition of hexanes and rotary evaporation gave **1** as a dry red solid (120 mg, 52%). Reduced reaction times may be achieved with only a slight reduction in the yield (45% *vs.* 52%) by carrying out the reaction in refluxing xylene (140 °C) for 1 d. **1** can also be prepared by heating a mixture of $\{Fe_2(CO)_5(\mu\text{-pdt})\}_2(\mu\text{-}\kappa^1,\kappa^1\text{-dppf})$ (**X**) and dppf in toluene over *ca.* 5 d. Characterising data for **1**: IR ν(CO)(CH_2Cl_2) 1986s, 1949vs, 1918s 1896w cm^{-1}. ^{1}H NMR ($CDCl_3$) δ 8.01 (t, *J* 8.2, 2H, Ph), 7.67–6.99 (m, 18H, Ph), 4.93 (brs, 2H, CH), 4.46 (s, 2H, CH), 4.44 (s, 2H, CH), 4.01 (s, 2H, CH), 2.60 (br, 2H, CH_2), 2.31 (m, 2H, CH_2), 2.13 (br, 2H, CH_2). $^{31}P\{^1H\}$ NMR ($CDCl_3$) 51.3 (s) ppm. Elemental analysis calc. for $Fe_3S_2P_2O_4C_{41}H_{34}\cdot 0.5CH_2Cl_2$ (found): C 54.16 (53.41), H 3.81 (3.75).

Synthesis of $Fe_2(CO)_4(\mu\text{-dcpf})(\mu\text{-pdt})$ (2). $Fe_2(CO)_6(\mu\text{-pdt})$ (225 mg, 0.585 mmol) and dcpf (180 mg, 0.585 mmol) were refluxed in xylene (30 ml) for 16 h. Volatiles were removed under reduced pressure and impurities removed by dissolving in warm MeCN followed by filtration and recrystallisation at 4 °C. After extensive washing of the solid with cold hexane **2** was isolated as a dark brown powder (290 mg, 55%). Characterising data for **2**: IR ν(CO)(CH_2Cl_2) 1974s, 1934vs, 1903s, 1879w cm^{-1}. ^{1}H NMR ($CDCl_3$) δ 4.41–4.12 (8H, Fc), 2.50–2.32 (6H, pdt), 2.56–1.21 (44 H, Cy). $^{31}P\{^1H\}$ (d^8-toluene)

(353 K): δ 62.5 (s) ppm. HRMS (ESI/QTOF) m/z: $[M]^+$ calcd for $C_{41}H_{58}Fe_3O_4P_2S_2$: 908.13; found: 908.128.

Attempted synthesis of $Fe_2(CO)_4$(μ-dipf)(μ-pdt). $Fe_2(CO)_6$(μ-pdt) (100 mg, 0.26 mmol) and dipf (120 mg, 0.28 mmol) were refluxed in xylene for 16 h. Solvents were removed under reduced pressure. The resultant solid was very prone to oxidation. Attempts to purify by chromatography on silica led to significant degradation, while washing with hexanes and MeCN did not give a clearer product. Following these washings and drying under vacuum the product was tentatively identified on the basis of the following data. ^{1}H NMR: ($CDCl_3$) δ 5.30, 4.66, 4.46, 4.27 (s, 8H, Cp), 3.46–3.50 (q, 2H, CH_2), 2.38–2.55 (t, 4H, CH_2), 1.59–1.26 (m, 28H, i-Pr). IR ν(CO) CH_2Cl_2: 1970s, 1936vs, 1904s, 1880w cm^{-1}.

Synthesis of $Fe_2(CO)_4$(μ-dppf)(μ-edt) (3). $Fe_2(CO)_6$(μ-edt) (0.20 g, 0.54 mmol) and dppf (0.60 g, 1.08 mmol) in xylene (20 ml) were refluxed for 24 h resulting in a colour change from orange to red-brown. After cooling to room temperature, volatiles were removed under reduced pressure to give a dark red residue. This was washed with hexanes (30 ml) and dried. Then the residue was chromatographed by TLC on silica gel. Elution with hexane/CH_2Cl_2 (1 : 2, v/v) developed five bands. The fastest moving band gave unreacted dppf. The second major band gave red crystals of $Fe_2(CO)_4$(μ-edt)(μ-dppf) (**3**) (93 mg, 20%) after recrystallisation from n-hexane/CH_2Cl_2 at 4 °C. The contents of other bands were too small for complete characterisation. Characterising data for **3**: IR ν(CO)(CH_2Cl_2): 1989s, 1952vs, 1921s, 1900w cm^{-1}. ^{1}H NMR ($CDCl_3$): δ 7.96 (t, J 8.0, 2H, Ph), 7.43–7.37 (m, 14H, Ph), 7.28 (s, 2H, Ph), 4.81 (s, 2H, CH), 4.45 (s, 2H, CH), 4.37 (s, 2H, CH), 3.98 (s, 2H, CH), 2.77 (br, s, 2H, CH_2), 2.33 (br, s, 2H, CH_2). ^{31}P{H} NMR ($CDCl_3$): δ 54.9 (s) ppm. ESI-MS: m/z 870.95 (M + H^+, 10%), 841.94 (M − CO, 30%), 813.94 (M − 2CO, 30%), 757.96 (M − 4CO, 30%), 702.13 (100%). Elemental analysis. Calcd (found): $C_{40}H_{32}Fe_3O_4P_2S_2{\cdot}C_6H_{14}$: C 57.78 (57.24), H 4.81 (4.24).

Synthesis of $Fe_2(CO)_4(\mu\text{-SPh})_2$(μ-dppf) (4a). A xylene solution of $Fe_2(CO)_6(\mu\text{-SPh})_2$ (0.15 g, 0.30 mmol) and dppf (0.17 g, 0.31 mmol) was heated for 30 min 145 °C. The reaction mixture turned dark red. Upon cooling, the volatiles were removed under reduced pressure. The residue was chromatographed by TLC on silica gel. Elution with hexane/CH_2Cl_2 (1 : 1) developed two bands in addition to the starting material, the major band being $Fe_2(CO)_4(\mu\text{-SPh})_2$(μ-dppf) (**4a**) (0.042 g, 0.04 mmol, 14% yield). Recrystallisation from a CH_2Cl_2–hexane mixture afforded crystals suitable for X-ray diffraction. Characterising data for **4a**: IR ν(CO) (CH_2Cl_2) 1990m, 1956vs, 1927s, 1902w cm^{-1}. ^{1}H NMR ($CDCl_3$) δ 8.19–6.99 (m, 30H, Ph), 4.99 (s, 2H, Cp), 4.52 (d, J 15.1, 4H, Cp), 4.06 (s, 2H, Cp). ^{31}P{^{1}H} NMR ($CDCl_3$) δ 52.4 (s). Elemental analysis calc. for $Fe_3S_2P_2O_4C_{50}H_{38}{\cdot}C_6H_{14}$ (found): C 62.11 (61.61), H 4.81 (4.67). $Fe_2(CO)_4(\mu\text{-STol})_2$(μ-dppf) (**4b**) (54%) was prepared in a similar manner. Characterising data for **4b**: IR ν(CO)(CH_2Cl_2) 1989m, 1964vs, 1925s, 1902w cm^{-1}. ^{1}H NMR ($CDCl_3$) δ 8.17–6.80 (m, 28H, Ph), 4.99 (s, 2H, Cp), 4.52 (d, J 18.0, 4H, Cp), 4.06 (s, 2H, Cp), 2.36 (s, 3H, CH_3), 2.14 (s, 3H, CH_3). ^{31}P{^{1}H} NMR ($CDCl_3$) δ 52.4 (s). Elemental analysis calc. for $Fe_3S_2P_2O_4C_{52}H_{42}{\cdot}C_6H_{14}$ (found): C 62.70 (61.79), H 5.05 (4.85).

Synthesis of $Fe_2(CO)_4(\mu\text{-SC}_6H_4NH_2)$(μ-dppf) (4c). A xylene solution of $Fe_2(CO)_6(\mu\text{-SC}_6H_4NH_2)$ (0.16 g, 0.30 mmol) and dppf (0.17 g, 0.31 mmol) was heated for 40 min at 120 °C and a further 20 min at 140 °C. The reaction mixture turned dark red. Upon cooling, the volatiles were removed under reduced pressure. The residue was washed with hexane, dissolved in a minimum amount of CH_2Cl_2 and filtered through Celite. The major product was identified as $Fe_2(CO)_4(\mu\text{-SC}_6H_4NH_2)_2$(μ-dppf) (**4c**) (0.039 g, 0.04 mmol, 13% yield) being recrystallised from a CH_2Cl_2–MeOH mixture. Characterising data for **4c**: IR ν(CO)(CH_2Cl_2) 1987m, 1952vs, 1923s, 1898w cm^{-1}. ^{1}H NMR ($CDCl_3$) δ 8.13 (t, J 7.6, 4H, Ph), 7.60–7.39 (m, 18H, Ph), 7.05 (d, J 6.9, 2H, Ph), 6.72 (d, J 5.0, 2H, Ph), 6.38 (d, 6.0, 2H, Ph), 4.97 (s, 2H, Cp), 4.50 (d, J 14.4, 4H, Cp), 4.04 (s, 2H, Cp), 2.72 (br, NH_2). ^{31}P{^{1}H} NMR ($CDCl_3$) δ 52.2 (s). Elemental analysis calc. for $Fe_3S_2P_2O_4N_2C_{50}H_{40}$ (found): C 53.96 (53.62), H 3.60 (3.65).

Synthesis of $[Fe_2(CO)_4(\mu\text{-H})(\mu\text{-dppf})(\mu\text{-pdt})][BF_4]$[1H][$BF_4$]. To a CH_2Cl_2 (50 ml) solution of **1** (0.150 g, 0.17 mmol) was added a few drops of HBF_4. The mixture was stirred at room temperature for 20 min without any noticeable change to the colour. Volatiles were removed under reduced pressure and the resulting deep red oily solid washed with a small portion of Et_2O to remove excess acid. The remaining solid was dissolved in a minimum amount of CH_2Cl_2 which was then layered with hexanes. Slow mixing of the solutions afforded [**1H**][BF_4] as a dry red solid (120 mg, 73%). Characterising data for **1H$^+$**: IR ν(CO)(CH_2Cl_2) 2058s, 2040s, 2002s cm^{-1}. ^{1}H NMR ($CDCl_3$) δ 8.11–7.33 (m, 20H, Ph), 4.74 (s, 2H, CH), 4.68 (s, 2H, CH), 4.49 (s, 2H, CH), 4.32 (s, 2H, CH), 2.86 (br, 2H, CH_2), 2.74 (m, 2H, CH_2), 2.48 (br, 2H, CH_2), −12.40 (t, J 17.6, 1H, μ-H). ^{31}P{^{1}H} NMR (CD_2Cl_2) 44.8 (s) ppm.

Synthesis of $[Fe_2(CO)_4(\mu\text{-H})(\mu\text{-dcpf})(\mu\text{-pdt})][BF_4]$[2H][$BF_4$]. In an NMR tube under N_2 a small amount of $HBF_4{\cdot}Et_2O$ was added to **2** (0.015 g) in CD_2Cl_2 (*ca.* 0.8 ml) solution. The solution immediately darkened, and changes were followed by ^{1}H and ^{31}P{^{1}H} NMR spectroscopy. Characterising data for **2H$^+$**: IR ν(CO)(CH_2Cl_2) 2054m, 2034s, 1975s cm^{-1}. ^{1}H NMR (CD_2Cl_2) δ −13.4 (br, 1H, μ-H). ^{31}P{^{1}H} NMR (CD_2Cl_2) 53.3 (brs) ppm.

X-ray structure determinations

For **1**, **4a** and **4c**, single crystals were mounted on a glass fiber and all geometric and intensity data were taken from this sample using a Bruker SMART APEX CCD diffractometer using graphite-monochromated Mo-K_α radiation (λ = 0.71073 Å) at 150 ± 2 K. Data reduction were carried out with SAINT PLUS[47] and absorption corrections applied using the programme SADABS.[48] Structures were solved by direct methods and developed using alternating cycles of least-squares refinement and difference-Fourier synthesis. All non-hydrogen atoms were refined anisotropically. Hydrogens were placed in calculated positions (riding model). Structure solution used SHELXTL PLUS V6.10 program package.[49] For **3**, a single crystal was mounted on a MiTeGen loop on an XtaLAB AFC11 (RCD3) quarter-chi single diffractometer. The crystal was kept at 100.00(11) K during data collection using Cu-K_α radiation (λ =

1.54184 Å). Using Olex2,[50] the structure was solved with the olex2.solve[50] structure solution program using Charge Flipping and refined with the SHELXL[51] refinement package using Least Squares minimisation. Details of data collection and structure refinement are given in Table 1.[52] For **4a** voids in the initial structure solution were treated with the Olex implementation of the SQUEEZE function is Platon. Unfortunately it was not possible to model this as a disordered hexane although this is what we anticipate is present and is in accord with the elemental analysis results.

Electrochemical and spectroelectrochemical studies

Electrochemistry was carried out in deoxygenated acetonitrile or dichloromethane solutions with 0.1 M $TBAPF_6$ as the supporting electrolyte. The working electrode was a 3 mm diameter glassy carbon electrode that was polished with 0.3 μm alumina slurry prior to each scan. The counter electrode was a Pt wire and the quasi-reference electrode was a silver wire. All CVs were referenced to the Fc^+/Fc redox couple. An Autolab potentiostat (EcoChemie, Netherlands) was used for all CV experiments and an EmStat3 (Palmsens, Netherlands) potentiostat for IR-SEC experiments. Catalysis studies were carried out by adding equivalents of $HBF_4{\cdot}Et_2O$ or CF_3CO_2H (Sigma-Aldrich) for proton reduction and pyridine (Sigma-Aldrich) for dihydrogen oxidation. Spectroelectrochemical (SEC) measurements were conducted within an optically transparent thin-layer electrochemical (OTTLE) cell (Spectroelectrochemistry Reading). The OTTLE cell was equipped with a Pt mini-grid working electrode, a Pt counter electrode, a Ag wire pseudo-reference electrode, and CaF_2 windows. SEC samples contained 3×10^{-1} M TBAH as a supporting electrolyte. IR SEC ($\tilde{\nu}$ < 7500 cm^{-1}) was run on a Bruker Vertex 70v Fourier transform infrared spectrometer equipped with a DTLaGS detector.

Computational methodology

The DFT calculations reported here were performed with the Gaussian 09 package of programs.[53] The calculations were carried out with the B3LYP functional, which utilises the Becke three-parameter exchange functional (B3)[54] combined with the correlation functional of Lee, Yang, and Parr (LYP).[55] The iron

Table 2 Selected structural parameters

	1 [ref. 8]	**3**	**4a**	**4c**
Fe–Fe	2.6133(6)	2.6289(13)	2.6267(4)	2.6268(6)
Fe–P	2.2256(6)	2.2556(17)	2.2434(6)	2.2608(8)
	2.2679(6)	2.2595(19)	2.2584(5)	2.2463(8)
Fe–S_{cis}	2.2540(6)	2.2491(19)	2.2553(5)	2.2744(8)
	2.2565(6)	2.2354(16)	2.2792(5)	2.2495(7)
Fe–S_{trans}	2.2410(6)	2.2353(17)	2.2552(6)	2.2759(8)
	2.2508(6)	2.2421(18)	2.2792(5)	2.2553(7)
Fe···Fe	4.613(1)	4.493(1)	4.579(1)	4.581(1)
	4.581(1)	4.618(1)	4.586(1)	4.605(1)
Fe–Fe–P	120.10(2)	115.79(6)	119.06(2)	118.22(2)
	118.65(2)	120.16(6)	118.72(2)	119.24(2)
Fe–S(1)–Fe	71.15(2)	71.91(5)	70.80(2)	70.99(2)
Fe–S(2)–Fe	70.81(2)	71.78(5)	70.99(2)	70.86(2)
P–Fe–Fe–P	14.12(4)	22.28(8)	13.41(8)	14.70(5)

Table 1 Crystallographic data and structure refinement

Compound	**1**·0.5CH_2Cl_2 [ref. 8]	**3**	**4a**	**4c**
Empirical formula	$C_{41.50}H_{35}ClFe_3O_4P_2S_2$	$C_{40}H_{32}Fe_3O_4P_2S_2$	$C_{50}H_{38}Fe_3O_4P_2S_2$	$C_{50}H_{40}Fe_3N_2O_4P_2S_2$
Formula weight	926.75	870.26	996.41	1026.45
Temperature (K)	150	100	150	150
Crystal system	Triclinic	Monoclinic	Triclinic	Triclinic
Space group	$P\bar{1}$	$P2_1/n$	$P\bar{1}$	$P\bar{1}$
a (Å)	9.7365(19)	15.4691(8)	11.7727(4)	12.2875(6)
b (Å)	13.149(3)	11.0407(8)	12.3881(3)	12.6980(6)
c (Å)	16.654(3)	22.8109(10)	18.5833(3)	18.6853(9)
α (°)	99.609(3)	90	76.239(2)	79.137(4)
β (°)	94.376(3)	106.043(4)	79.887(2)	74.698(4)
γ (°)	111.343(3)	90	82.837(3)	83.481(4)
Volume (Å^3)	1936.1(7)	3744.1(3)	2581.76(12)	2755.3(2)
Z	2	4	2	2
$D_{calc.}$ (Mg m^{-3})	1.588	1.544	1.282	1.237
μ (Mo K_α) (mm^{-1})	1.411	11.381	1.013	0.953
F(000)	944	1776	1020	1052
Crystal size (mm)	0.38 × 0.32 × 0.16	0.15 × 0.08 × 0.02	0.23 × 0.19 × 0.12	0.22 × 0.19 × 0.15
θ range (°)	2.59–28.35	3.09–70.27	2.78–26.00	3.51–29.25
Limiting indices	$-12 \le h \ge 12$, $-17 \le k \ge 17$, $-21 \le l \ge 21$	$-18 \le h \ge 17$, $-13 \le k \ge 13$, $-22 \le l \ge 27$	$-14 \le h \ge 12$, $-15 \le k \ge 11$, $-22 \le l \ge 17$	$-16 \le h \ge 16$, $-12 \le k \ge 16$, $-24 \le l \ge 22$
Reflections collected	16 800	21 109	17 867	18 816
Independent reflections (R_{int})	8886 (0.0333)	6780 (0.0756)	11 779 (0.0239)	12 487 (0.0331)
Data/restraints/parameters	8886/0/511	6780/0/460	11 779/0/550	12 487/0/569
Goodness of fit on F^2	1.049	1.029	1.024	1.039
Final R indices [$I > 2\sigma(I)$]	R_1 = 0.0345, wR_2 = 0.0911	R_1 = 0.0722, wR_2 = 0.1740	R_1 = 0.0349, wR_2 = 0.0729	R_1 = 0.0492, wR_2 = 0.1129
R indices (all data)	R_1 = 0.0374, wR_2 = 0.0929	R_1 = 0.0941, wR_2 = 0.1864	R_1 = 0.0474, wR_2 = 0.0799	R_1 = 0.0661, wR_2 = 0.1228
Largest difference in peak and hole (e Å^{-3})	0.597 and −0.725	1.35 and −0.73	0.43 and −0.37	0.73 and −0.49

atoms were described by Stuttgart-Dresden effective core potentials (ecp) and SDD basis set, while the 6-31G(d') basis set was employed for the remaining atoms. The geometry-optimised structures reported here represent minima based on zero imaginary frequencies (positive eigenvalues) in the Hessian matrix. Unscaled vibrational frequencies were used to make zero-point and thermal corrections to the electronic energies. The geometry-optimised structures have been drawn with the JIMP2 molecular visualisation and manipulation program.[56]

Conflicts of interest

There are no conflicts to declare.

Acknowledgements

We thank the Commonwealth Scholarship Commission for the award of Commonwealth Scholarships (SG and JCS) and King's College London (GRFO) for PhD funding. GH thanks The Royal Society of Chemistry for an International Authors Grant which allowed this work to be developed during his visit to the University of North Texas and King's College London for funding. We thank Dr Nathan Patmore (University of Huddersfield) for some early IR-SEC on **1**, Professor Katherine J. Holt (UCL) for the initial electrochemical study on **1**, Dr Nathan Hollingsworth (ex-UCL) for part supervision of LA, and Kishan Muthu (KCL) for early attempts to prepare **2** while working under the supervision of GRFO. MGR acknowledges financial support from the Robert A. Welch Foundation (Grant B-1093-MGR). Computational resources through the High-Performance Computing Services and CASCaM at the University of North Texas are acknowledged. Dr David A. Hrovat is thanked for the generation of the spin density plots of **B** and ^{3}**C**. The experimental work in Reading was conducted with the support from Spectroelectrochemistry Reading, a spinout company of the University.

References

1 C. Sommer, A. Adamska-Venkatesh, K. Pawlak, J. A. Birrell, O. Rűdiger, E. J. Reijerse and W. Lubitz, *J. Am. Chem. Soc.*, 2017, **129**, 1440–1443.

2 F. Wittkamp, M. Senger, S. T. Stripp and U.-P. Apfel, *Chem. Commun.*, 2018, **54**, 5934–5942.

3 V. S. Thoi, Y. Sun, J. R. Long and C. J. Chang, *Chem. Soc. Rev.*, 2013, **42**, 2388–2400.

4 For reviews of this area see: (*a*) I. P. Georgakaki, L. M. Thomson, E. J. Lyon, M. B. Hall and M. Y. Darensbourg, *Coord. Chem. Rev.*, 2003, **238–239**, 255–266; (*b*) D. J. Evans and C. J. Pickett, *Chem. Soc. Rev.*, 2003, **32**, 268–287; (*c*) T. B. Rauchfuss, *Inorg. Chem.*, 2004, **43**, 14–26; (*d*) L. Sun, B. Åkermark and S. Ott, *Coord. Chem. Rev.*, 2005, **249**, 1653–1663; (*e*) X. Liu, S. K. Ibrahim, C. Tard and C. J. Pickett, *Coord. Chem. Rev.*, 2005, **249**, 1641–1652; (*f*) C. Tard and C. J. Pickett, *Chem. Rev.*, 2009, **109**, 2245–2274; (*g*) J.-F. Capon, F. Gloaguen, P. Schollhammer and J. Talarmin, *Coord. Chem. Rev.*, 2005, **249**, 1664–1676; (*h*) J.-F. Capon, F. Gloaguen, F. Y. Pétillon, P. Schollhammer and J. Talarmin, *Eur. J. Inorg. Chem.*, 2008, 4671–4681; (*i*) D. Schilter, J. M. Camara, M. T. Huynh, S. Hammes-Schiffer and T. B. Rauchfuss, *Chem. Rev.*, 2016, **116**, 8693–8749; (*j*) J. T. Kleinhaus, F. Wittkamp, S. Yadav, D. Siegmund and U.-P. Apfel, *Chem. Soc. Rev.*, 2021, **50**, 1668–1784; (*k*) F. Wittkamp, M. Senger, S. T. Stripp and U.-P. Apfel, *Chem. Commun.*, 2018, **54**, 5934–5942; (*l*) F. Arrigoni, L. Bertini, R. Breglia, C. Greco, L. De Gioia and G. Zampella, *New J. Chem.*, 2020, **44**, 17596–17615.

5 Y.-C. Liu, T.-H. Yen, K.-T. Chu and M.-H. Chiang, *Comments Inorg. Chem.*, 2016, **36**, 141–181.

6 C. Tard, X. Liu, S. K. Ibrahim, M. Bruschi, L. De Gioia, S. C. Davies, X. Yang, L.-S. Wang, G. Sawers and C. J. Pickett, *Nature*, 2005, **433**, 610–613.

7 (*a*) J. M. Camara and T. B. Rauchfuss, *Nat. Chem.*, 2012, **4**, 26–30; (*b*) J. C. Lansing, J. M. Camara, D. E. Gray and T. B. Rauchfuss, *Organometallics*, 2014, **33**, 5897–5906.

8 S. Ghosh, G. Hogarth, N. Hollingsworth, K. B. Holt, S. E. Kabir and B. E. Sanchez, *Chem. Commun.*, 2014, **50**, 945–947. CCDC 956914 (**1**).

9 (*a*) S. Ghosh, N. Hollingsworth, M. Warren, D. A. Hrovat, M. G. Richmond and G. Hogarth, *Dalton Trans.*, 2019, **48**, 6051–6060; (*b*) Y. Si, K. Charreteur, J.-F. Capon, F. Gloaguen, F. Y. Pétillon, P. Schollhammer and J. Talarmin, *J. Inorg. Biochem.*, 2010, **104**, 1038–1042; (*c*) S. Ghosh, S. Rana, N. Hollingsworth, M. G. Richmond, S. E. Kabir and G. Hogarth, *Inorganics*, 2018, **6**, 122; (*d*) R. Becker, S. Amirjalayer, P. Li, S. Wouterse and J. N. H. Reek, *Sci. Adv.*, 2016, **2**, e1501014; (*e*) Y.-C. Liu, C.-H. Lee, G.-H. Lee and M.-H. Chiang, *Eur. J. Inorg. Chem.*, 2011, 1155–1162.

10 (*a*) S. Ghosh, A. Rahaman, K. B. Holt, E. Nordlander, M. G. Richmond, S. E. Kabir and G. Hogarth, *Polyhedron*, 2016, **116**, 127–135; (*b*) S. Roy, T. L. Groy and A. K. Jones, *Dalton Trans.*, 2013, **42**, 3843–3853; (*c*) S. Roy, J. A. Laureanti, T. L. Groy and A. K. Jones, *Eur. J. Inorg. Chem.*, 2017, **2017**, 2942–2950; (*d*) P.-Y. Orain, J.-F. Capon, N. Kervarec, F. Gloaguen, F. Pétillon, R. Pichon, P. Schollhammer and J. Talarmin, *Dalton Trans.*, 2007, 3754–3756; (*e*) J. Zhao, Z. Wei, X. Zeng and X. Liu, *Dalton Trans.*, 2012, **41**, 11125–11133; (*f*) Y.-C. Liu, T.-H. Yen, Y.-J. Tseng, C.-H. Hu, G.-H. Lee and M.-H. Chiang, *Inorg. Chem.*, 2012, **51**, 5997–5999.

11 C. Nataro, A. N. Campbell, M. A. Ferguson, C. D. Incarvito and A. L. Rheingold, *J. Organomet. Chem.*, 2003, **673**, 47–55.

12 J. W. Tye, M. B. Hall and M. Y. Darensbourg, *Inorg. Chem.*, 2006, **45**, 1552–1559.

13 (*a*) F. I. Adam, G. Hogarth, I. Richards and B. E. Sanchez, *Dalton Trans.*, 2007, 2495–2498; (*b*) S. Ghosh, G. Hogarth, N. Hollingsworth, K. B. Holt, I. Richards, M. G. Richmond, B. E. Sanchez and D. Unwin, *Dalton Trans.*, 2013, **42**, 6775–6792.

14 X.-F. Liu and B.-S. Yin, *J. Coord. Chem.*, 2010, **63**, 4061–4067.
15 C.-G. Li, F. Xue, M.-J. Cui, J.-Y. Shang and T.-J. Lou, *Transition Met. Chem.*, 2015, **40**, 47–52.
16 H. Li, Q. Gong, X. Chai, C. Yao and Q. Han, *Asian J. Chem.*, 2015, **27**, 1553–1554.
17 X.-F. Liu, Z.-Q. Jiang and Z.-J. Jia, *Polyhedron*, 2012, **33**, 166–170.
18 F. I. Adam, G. Hogarth and I. Richards, *J. Organomet. Chem.*, 2007, **692**, 3957–3968.
19 S. Rana, S. Ghosh, Md. K. Hossain, A. Rahaman, G. Hogarth and S. E. Kabir, *Transition Met. Chem.*, 2016, **41**, 933–942.
20 F. I. Adam, G. Hogarth, S. E. Kabir and I. Richards, *C. R. Chim.*, 2008, **11**, 890–905.
21 G. Hogarth, M. O'Brien and D. A. Tocher, *J. Organomet. Chem.*, 2003, **672**, 29–33.
22 C.-G. Li, S.-L. Wang and J.-Y. Shang, *J. Coord. Chem.*, 2016, **69**, 2845–2854.
23 N. Begum, U. K. Das, M. Hassan, G. Hogarth, S. E. Kabir, E. Nordlander, M. A. Rahman and D. A. Tocher, *Organometallics*, 2007, **26**, 6462–6472.
24 (*a*) X. L. Lu, S. Y. Ng, J. J. Vittal, G. K. Tan, L. Y. Goh and T. S. A. Hor, *J. Organomet. Chem.*, 2003, **688**, 100–111; (*b*) D. Cauzzi, C. Graiff, C. Massera, G. Predieri, A. Tiripiccho and D. Acquotti, *J. Chem. Soc., Dalton Trans.*, 1999, 3515–3521.
25 (*a*) G. Hogarth and I. Richards, *Inorg. Chem. Commun.*, 2007, **10**, 66–70; (*b*) G. M. Chambers, R. Angamuthu, D. L. Gray and T. B. Rauchfuss, *Organometallics*, 2013, **32**, 6324–6329; (*c*) D. Schilter, M. J. Nilges, M. Chakrabarti, P. A. Lindahl, T. B. Rauchfuss and M. Stein, *Inorg. Chem.*, 2012, **51**, 2338–2348.
26 G. Hogarth, S. E. Kabir and I. Richards, *Organometallics*, 2010, **29**, 6559–6568.
27 S. Ghosh, B. E. Sanchez, I. Richards, M. N. Haque, K. B. Holt, M. G. Richmond and G. Hogarth, *J. Organomet. Chem.*, 2016, **812**, 247–258.
28 (*a*) A. C. Ohs, A. L. Rheingold, M. J. Shaw and C. Nataro, *Organometallics*, 2004, **23**, 4655–4660; (*b*) M. R. Ringenberg, M. Schwilk, F. Wittkamp, U.-P. Apfel and W. Kaim, *Chem. – Eur. J.*, 2017, **23**, 1770–1774; (*c*) M. R. Ringenberg and F. Döttinger, *Eur. J. Inorg. Chem.*, 2019, **2019**, 2430–2435.
29 (*a*) M. E. Carroll, B. E. Barton, T. B. Rauchfuss, P. J. Carroll and J. Am, *Chem. Soc.*, 2012, **134**, 18843–18852; (*b*) G. Eilers, L. Schwartz, M. Stein, G. Zampella, L. De Gioia, S. Ott and R. Lomoth, *Chem. – Eur. J.*, 2007, **13**, 7075–7084.
30 M. Häßner, J. Fiedler and M. R. Ringenberg, *Inorg. Chem.*, 2019, **58**, 1742–1745.
31 F. Arrigoni, L. Bertini, M. Bruschi, C. Greco, L. De Gioia and G. Zampella, *Chem. – Eur. J.*, 2019, **25**, 1227–1241.
32 (*a*) S. Ezzaher, J.-F. Capon, F. Gloaguen, F. Y. Petillon, P. Schollhammer, J. Talarmin, R. Pichon and N. Kervarec, *Inorg. Chem.*, 2007, **46**, 3426–3428; (*b*) S. Ezzaher, J.-F. Capon, N. Dumontet, F. Gloaguen, F. Y. Petillon, P. Schollhammer and J. Talarmin, *J. Electroanal. Chem.*, 2009, **626**, 161–170; (*c*) C. Greco, P. Fantucci, L. De Gioia, R. Suarez-Bertoa, M. Bruschi, J. Talarmin and P. Schollhammer, *Dalton Trans.*, 2010, **39**, 7320–7329; (*d*) B. E. Barton, G. Zampella, A. K. Justice, L. De Gioia, T. B. Rauchfuss and S. R. Wilson, *Dalton Trans.*, 2010, **39**, 3011–3019.
33 W. Gao, J. Ekström, J. Liu, C. Chen, L. Eriksson, L. Weng, B. Akermark and L. Sun, *Inorg. Chem.*, 2007, **46**, 1981–1991.
34 T. Agarwal and S. Kaur-Ghumaan, *Coord. Chem. Rev.*, 2019, **397**, 188–219.
35 G. A. N. Felton, R. S. Glass, D. L. Lichtenberger and D. H. Evans, *Inorg. Chem.*, 2006, **45**, 9181–9184.
36 R. Mejia-Rodriguez, D. Chong, J. H. Reibenspies, M. P. Soriaga and M. Y. Darensbourg, *J. Am. Chem. Soc.*, 2004, **126**, 12004–12014.
37 A. Jabloskyté, J. A. Wright, S. A. Fairhurst, J. N. T. Peck, S. K. Ibrahim, V. S. Oganesyan and C. J. Pickett, *J. Am. Chem. Soc.*, 2011, **133**, 18606–18609.
38 W. Wang, M. J. Nilges, T. B. Rauchfuss and M. Stein, *J. Am. Chem. Soc.*, 2103, **135**, 3633–3639.
39 G. Filippi, F. Arrigoni, L. Bertini, L. De Gioia and G. Zampella, *Inorg. Chem.*, 2105, **54**, 9529–9542.
40 N. Wang, M. Wang, Y. Wang, D. Zheng, H. Han, M. S. G. Ahlquist and L. Sun, *J. Am. Chem. Soc.*, 2013, **135**, 13688–13691.
41 F. Arrigoni, L. Bertini, R. Breglia, C. Greco, L. De Gioia and G. Zampella, *New J. Chem.*, 2020, **44**, 17596–17615.
42 J. W. Peters, W. N. Lanzilotta, B. J. Lemon and L. C. Seefeldt, *Science*, 1998, **282**, 1853–1858.
43 A. Winter, L. Zsolnai and G. Huttner, *Z. Naturforsch., B: Anorg. Chem., Org. Chem.*, 1982, **37**, 1430–1436.
44 P. C. Ellgen and J. N. Gerlach, *Inorg. Chem.*, 1973, **12**, 2526–2532.
45 A. L. Haley, L. N. Broadbent, L. S. McDaniel, S. T. Heckman, C. H. Hinkle, N. N. Gerasimchuk, J. C. Hershberger and C. A. Mebi, *Polyhedron*, 2016, **114**, 218–224.
46 C. A. Mebi, D. S. Karr and R. Gao, *J. Coord. Chem.*, 2011, **64**, 4397–4407.
47 *SAINT Version 6.36A*, Bruker AXS, Inc., Analytical X-ray Systems, 5465 East Cheryl Parkway, Madison WI 53711-5373, 2002.
48 G. M. Sheldrick, *SADABS Version 2.10*, University of Göttingen, 2003.
49 G. M. Sheldrick, *Acta Crystallogr., Sect. A: Found. Crystallogr.*, 2008, **A64**, 112–122.
50 O. V. Dolomanov, L. J. Bourhis, R. J. Gildea, J. A. K. Howard and H. Puschmann, *J. Appl. Crystallogr.*, 2009, **42**, 339–341.
51 L. J. Bourhis, O. V. Dolomanov, R. J. Gildea, J. A. K. Howard and H. Puschmann, *Acta Crystallogr., Sect. A: Found. Adv.*, 2015, **A71**, 59–75.
52 G. M. Sheldrick, *Acta Crystallogr., Sect. C: Struct. Chem.*, 2015, **C71**, 3–8.

53 M. J. Frisch, *et al.*, *Gaussian 09, Revision E.01*, Gaussian, Inc., Wallingford, CT, USA, 2009.
54 A. D. Becke, *J. Chem. Phys.*, 1993, **98**, 5648–5652.
55 C. Lee, W. Yang and R. G. Parr, *Phys. Rev. B: Condens. Matter Mater. Phys.*, 1993, **37**, 785–789.
56 (*a*) *JIMP2, version 0.091, a free program for the visualisation and manipulation of molecules*; M. B. Hall and R. F. Fenske, *Inorg. Chem.*, 1972, **11**, 768–775(*b*) J. Manson, C. E. Webster and M. B. Hall, Texas A&M University, College Station, TX, 2006, **https://www.chem.tamu.edu/jimp2/index.html**.